PHOTONICS Research

Polarization singularities in planar electromagnetic resonators with rotation and mirror symmetries

Jie Yang,[1,2] Xuezhi Zheng,[1,4] Jiafu Wang,[2,5] Anxue Zhang,[2] Tie Jun Cui,[3] and Guy A. E. Vandenbosch[1]

[1]WaveCoRE Research Group, KU Leuven, Leuven B-3001, Belgium
[2]Xi'an Jiaotong University, Xi'an 710049, China
[3]State Key Laboratory of Millimeter Wave, Southeast University, Nanjing 210096, China
[4]e-mail: xuezhi.zheng@esat.kuleuven.be
[5]e-mail: wangjiafu1981@126.com

Received 13 January 2023; revised 2 March 2023; accepted 3 March 2023; posted 6 March 2023 (Doc. ID 485625); published 16 May 2023

In this work, we apply the group representation theory to systematically study polarization singularities in the in-plane components of the electric fields supported by a planar electromagnetic (EM) resonator with generic rotation and reflection symmetries. We reveal the intrinsic connections between the symmetries and the topological features, i.e., the spatial configuration of the in-plane fields and the associated polarization singularities. The connections are substantiated by a simple relation that links the topological charges of the singularities and the symmetries of the resonator. To verify, a microwave planar resonator with the D_8 group symmetries is designed and numerically simulated, which demonstrates the theoretical findings well. Our discussions can be applied to generic EM resonators working in a wide EM spectrum, such as circular antenna arrays, microring resonators, and photonic quasi-crystals, and provide a unique symmetry perspective on many effects in singular optics and topological photonics.

https://doi.org/10.1364/PRJ.485625

1. INTRODUCTION

An electromagnetic (EM) singularity refers to a point in space where a physical parameter of the EM field is undefined, which gives rise to nontrivial topologies of the field [1–6]. The EM singularities as topological defects have provided a unique perspective for connecting many fundamental concepts, such as angular momenta of light [5–7], bound states in the continuum [8–11], EM multipoles [12–14], and optical chirality [15,16], and thus have become a central topic that covers a broad range of the EM spectrum from microwaves, via terahertz, to optical frequencies, in the research field of wave engineering [6,12,17,18]. There are two typical categories of singularities: the scalar and the vector singularities, also known as phase and polarization singularities. The phase singularity occurs in a scalar field where the intensity is zero and the phase is undefined. In the paraxial regime, an EM wave with the phase singularity is aliased as a vortex mode that has a homogeneous polarization pattern and carries an orbital angular momentum (OAM) of $l\hbar$ (l is the order of phase singularity or topological charge; $\hbar$ is the reduced Planck constant) [5,6,19]. The polarization singularity occurs in a vector field where a parameter characterizing polarization ellipse is undefined, such as orientation, handedness, or eccentricity [1,2,17]. An EM wave with the polarization singularity exhibits inhomogeneous polarization patterns. The manipulation of the polarization patterns with EM scatterers has been of importance in both classical and quantum optics and has fueled various applications, such as optical manipulation [20,21], optical information processing [22–24], engineering Bose–Einstein condensation [25], controlling single-quantum radiation [26], realizing optical quasiparticles [27–30], and designing EM devices beyond scalar optics limit [28,31–34].

In the study of phase and polarization singularities, the symmetries of EM scatterers always play a significant role. For example, rotational symmetries of the scatterers are closely related to the EM singularities [10,35–41]. This can be demonstrated by the fact that many devices with rotational symmetries have been proposed to generate scalar vortex modes with phase singularity and have facilitated a plethora of OAM-based applications ranging from classical to quantum regimes [42–45]. Accordingly, the relation between the symmetries and the phase singularity has been intensively studied [35–40]. Regarding the relation between the symmetries and the polarization singularities, symmetry analysis finds [46] that polarization singularities in one-dimensional (1D) and two-dimensional (2D) photonic crystals (PCs) can support bound states in the continuum

(BICs). For this case, to realize the BICs, aside from the translation symmetries and possible rotational symmetries in the PCs, the PCs are further required to hold the $C_2^z T$ and σ_z symmetries (in detail, the former is the rotation of 180 deg with respect to the axis perpendicular to the PCs together with the time reversal symmetry, while the latter is a reflection with respect to the mid-plane of the PCs). Also, a systematic study harnessing the group theoretical tool has been performed to study the polarization singularities in the momentum space of 2D photonic quasi-crystals [10]. However, both studies are carried out in the momentum space, and such relation in real space has not been clearly and systematically revealed.

In this work, we focus on a planar EM resonator with M rotational and M reflection symmetries (which form a D_M group), and apply the group representation theory to investigate the relations between the symmetries and the polarization singularities. This work results in two key conclusions: the first is encoded in Eqs. (4) and (5) in Section 2 and the second, i.e., the "symmetry-matching condition" in Section 3. The former relates the topological features of the polarization distributions supported by the resonator with the resonator's symmetries. This relation offers a neat way for designers interested in predicting accepted or forbidden topological charges of polarization singularities based on the symmetries of the underlying resonator. The latter provides a set of design rules that customizes the geometric parameters of a feeding network, so that the network can produce an incident field that excites a planar EM resonator to radiate polarization singularities with the desired topological charges. By this design rule, we design a microwave plasmonic resonator (MPR) with the D_8 group symmetries. The numerical simulations demonstrate our theoretical considerations well. Our approach can be readily extended to other EM systems working in a wide EM spectrum, such as chiral nanoemitter arrays [36,37], microring resonators [38,39], photonic quasi-crystals [21], and circular antenna arrays [35]. It can provide not only a unique symmetry perspective on many effects in singular optics and topological photonics, but also a generic symmetry approach towards devising, e.g., optical skyrmions [27,47], plasmonic merons [29], and photonic spin textures [28,30].

2. EIGEN ELECTRIC FIELDS IN A RESONATOR WITH THE D_M GROUP SYMMETRIES

The main conclusions of this section are Eqs. (4) and (5). To derive the conclusions, we start with reiterating several key observations on the irreducible representations (irreps) for the C_M group and the D_M group. Here, most importantly, we give an index, i.e., an integer j, to each dimension of the irreps of the groups. Then, we point out that each dimension of the irreps defines an eigen electric field distribution. By using a resonator with the D_8 group symmetries, we illustrate the polarization morphologies and the topological features of the eigen electric field distributions. Last but not least, because each dimension of the irreps 1) is given an integral index, i.e., j, and 2) defines an eigen electric field distribution holding very specific topological features, i.e., topological charges, we rigorously establish a relation between the indices j's and the topological charges in the eigen electric fields, i.e., Eqs. (4) and (5).

To streamline the text, the mathematical background and the mathematical derivations are put in the appendices. The mathematics behind Subsection 2.A is given in Appendix A, and the proofs for the relations are given in Appendix B.

A. Indexing the Irreps of the C_M and D_M Groups

Without loss of generality, we consider a planar metal resonator. The resonator has M-fold rotation and M-fold reflection symmetries. The rotations and the reflections form the D_M group. For further discussions, we note that the rotations form the C_M group, and the C_M group is a subgroup of the D_M group. For both the C_M and the D_M groups, M is an integer larger than or equal to 2. An example of a resonator with the D_8 group symmetries is illustrated in Fig. 1.

In the following, several important observations on the irreps of the C_M group and the D_M group are reiterated as follows [48]. For the C_M group, the main points are:

- When M is odd, the irreps of the C_M group have one 1D irrep, i.e., A, and $(M-1)/2$ 2D irreps, i.e., E_h, where h is an integer spanning from 1 to $(M-1)/2$.
- When M is even, the irreps of the C_M group have two 1D irreps, i.e., A and B, and $(M/2-1)$ 2D irreps, i.e., E_h, where h is an integer spanning from 1 to $M/2-1$.
- Each dimension of the irreps of the C_M group can be indexed by an integer j (see how the indices are stipulated in Appendix A). For the case that M is odd, A is indexed by $j=0$. For the case that M is even, A and B are indexed by $j=0$ and $j=M/2$, respectively. For both even and odd M's, the two dimensions of E_h are indexed by $j=h$ and $j=M-h$, respectively.

For the D_M group, the main points are:

- When M is odd, the irreps of the D_M group have two 1D irreps, i.e., A_1 and A_2. They originate from the 1D irrep A of the C_M subgroup. Accordingly, the A_1 and the A_2 irreps inherit the index $j=0$ from the A irrep of the C_M group.
- When M is even, the irreps of the D_M group have four 1D irreps, i.e., A_1, A_2 and B_1, B_2. The A_1 irrep and the A_2 irrep originate from the 1D irrep A of the C_M subgroup, while the B_1 irrep and the B_2 irrep are from the B irrep of the C_M

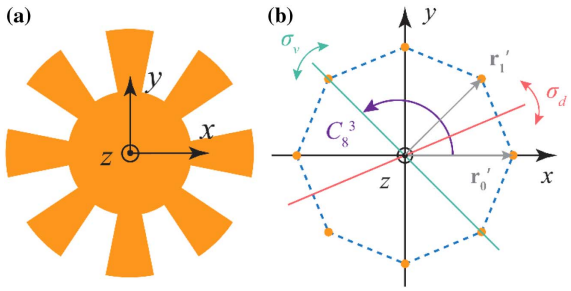

Fig. 1. Illustration of a resonator with eightfold rotation symmetries and eightfold reflection symmetries. These symmetries compose the D_8 group. In (a), the resonator (in orange) is assumed to be made of metal. The resonator in (a) is abstracted as eight points to demonstrate the symmetries [see the orange points in (b)]. In (b), three symmetries operations are given as examples: C_8^3, is a rotation by $3\pi/8$ with respect to the z axis (see the purple arrow); and σ_v and σ_d are reflections with respect to the planes made by the z axis and the green line, and by the z axis and the red line, respectively.

subgroup. As a result, A_1 and A_2 are indexed by $j = 0$, and B_1 and B_2 are indexed by $j = M/2$.

- For both even and odd M's, the 2D irreps E_h of the D_M group and their indices are the same as the C_M group case.

For the sake of completeness, the irreps of the C_M group and of the D_M group are presented in Tables 1–4 in Appendix A.

B. Singularities in Eigen Electric Fields

Based on the group representation theory [49], each dimension of the irreps defines an electric field distribution. The electric field distributions corresponding (belonging) to different dimensions of the irreps are orthonormal. Since the field distribution is only dependent on symmetries, it is called an "eigen electric field" (see the end of Appendix A for details).

To illustrate the eigen electric fields, we use the resonator (see Fig. 1), with the D_8 group symmetries as an example. For the out-of-plane component of the fields (see Fig. 2), i.e., E_z, the A_1 and the A_2 irreps demonstrate a trivial scalar vortex mode, i.e., a vortex mode with topological charge of 0, and a hexadecapole; the B_1 and B_2 irreps correspond to two octopoles which can be obtained by a rotation by $\pi/8$ of each other; and the E_1, E_2, E_3 irreps exhibit two scalar vortex modes with opposite topological charges of −1, +1, −2, +2, and −3, +3, respectively.

For the in-plane components (see Fig. 3), i.e., $\mathbf{E}_\parallel$, various polarization distributions are exhibited. For the A_1 and A_2 irreps, the vector fields in the distributions are radially and azimuthally oriented, respectively. Both distributions have V-type polarization singularities (i.e., V-point). By definition, a V-point is an intensity null point in a linearly polarized field [17]. At the V-point, the polarization azimuth is undefined. Further, the B_1 and B_2 irreps demonstrate vectorial octopole patterns. Both polarization distributions show a mix of the linear, the left-circular and the right-circular polarization states. Especially, for the B_1 and B_2 irreps, eight lines along radial directions segregate the regions of right-handedness from the ones of the left-handedness. Lastly, for an E_h ($h = 1, 2, 3$) irrep, the eigen electric fields are always left- (corresponding to the dimension indexed by $j = h$) and right-elliptically polarized (corresponding to the dimension indexed by $j = M - h$ and here $M = 8$). The fields always exhibit the so-called C-point singularities at which the orientation of the major axis of the polarization ellipse is undefined. The topological charges of the polarization distributions (marked in Fig. 3) can be evaluated by the synthesized Stokes fields of the in-plane components (see Appendix C).

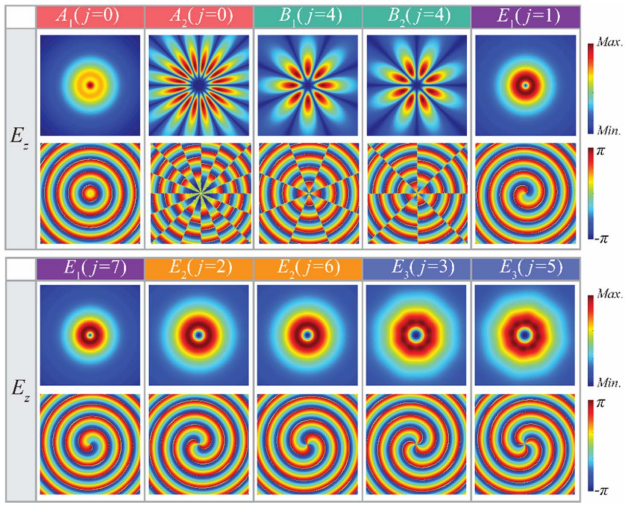

Fig. 2. Illustration of the magnitude and the phase distributions of the z component of the eigen electric fields. The colors in the figure are coded from blue to red to denote the strength and the phase variations. Unless otherwise stated, the same color coding will be applied to the rest of this work.

C. Relations between the Indices of the Irreps and the Topological Charges of Vortices

In the above example, the eigen electric fields clearly demonstrate topological features, i.e., the EM singularities and the associated topological charges. Since the eigen electric fields are always associated with the dimensions of the irreps of the D_M group, and each dimension of the irreps is indexed by an integer j, it is natural to establish a relation between the index j and the order of the topological charge. For the out-of-plane component, we have demonstrated in our previous work [50] that the topological charge of the scalar vortex (associated with E_z) is related to the index j,

$$l_z = \begin{cases} -j + Mq, & j < M/2 \\ M - j + Mq, & j > M/2 \end{cases}, \tag{1}$$

where q is an arbitrary integer. Equation (1) applies to both the odd M and the even M cases. Especially, when M is an even integer, the $j = M/2$ case exhibits the M-pole (see the B_1 and the B_2 cases in Fig. 2).

For the in-plane components carrying polarization singularities, considering that an EM wave with polarization singularity

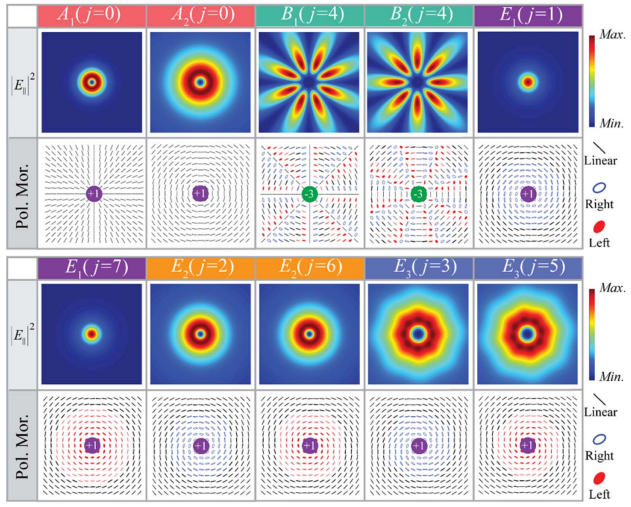

Fig. 3. Illustration of the intensity and the polarization distributions of the in-plane components of the eigen electric fields. In the figure, $|\mathbf{E}_\parallel|^2 = E_x^2 + E_y^2$, and "Pol. Mor." is an abbreviation of "polarization morphology." To describe the polarization morphologies, three symbols, i.e., the black lines, the blue hollow ellipses, and the red solid ellipses, are introduced to represent the linear, the right-handed, and the left-handed polarization states, respectively. The topological charges carried by the polarization vortices are marked at the centers of the polarization distributions.

can be seen as the superposition of two scalar vortices in orthogonal circular bases [17], we can express the field $\mathbf{E}_{\parallel}$ as

$$\mathbf{E}_{\parallel} = |E_L| e^{i l_L \varphi} \hat{L} + |E_R| e^{i l_R \varphi} e^{i\beta} \hat{R}. \quad (2)$$

In the above equation, $\hat{L} = \frac{1}{\sqrt{2}}(\hat{x} + i\hat{y})$ and $\hat{R} = \frac{1}{\sqrt{2}}(\hat{x} - i\hat{y})$ are the left and the right circular bases, respectively, l_L and l_R are the topological charges associated with the left and the right circular components, and β is the constant phase shift between the left and the right circular components. The order of the polarization singularity (or the topological charge) superposed by the left and the right circular vortices can be evaluated as [17]

$$I = (l_R - l_L)/2. \quad (3)$$

For the topological charges l_L and l_R, we prove (see the proofs in Appendix B) that the topological charges of the left and right scalar vortices (associated with E_L and E_R) are related to the index j,

$$l_L = -(j + 1 + q_L M), \qquad l_R = -(j - 1 + q_R M), \quad (4)$$

where q_L and q_R are arbitrary integers. Equation (4) can be further illustrated by the numerical results (see Appendix D for the D_8 group case). As a result of Eqs. (3) and (4), the topological charge of the polarization singularity is

$$I = 1 + (q_L - q_R)\frac{M}{2}. \quad (5)$$

When M is even, the main conclusions in Eq. (5) can be readily confirmed by the example in Fig. 3. That is, for the cases where $j \neq 4$, the choice of $M = 8$ and $q_L = q_R = 0$ leads to the topological charge of 1 (see Fig. 3); for the case $j = 4$, the choice of $M = 8$, $q_L = 0$, and $q_R = 1$ leads to the topological charge of −3 (see Fig. 3). Notably, in Fig. 3 both the A_1 and A_2 irreps are indexed by $j = 0$. But there is a difference between their polarization distributions. This difference originates from the constant phase shifts β in Eq. (2). For the A_1 irrep, the E_L and E_R components have no phase shift, i.e., $\beta = 0$, which results in the final polarization distribution being radially polarized. For the A_2 irrep, the E_L and E_R components have π phase shift, which results in the final polarization distribution being azimuthally polarized. Similar remarks apply to the B_1 irrep and the B_2 irrep as well (see Fig. 3). Notably, since q_L and q_R are always integers, a fractional-order polarization singularity is strictly forbidden for an even M.

To further confirm the above conclusions for the odd M case, the D_7 group case is shown in Appendix E. There, the B_1 irrep and the B_2 irrep do not exist. As a result, when q_L and q_R are zero, the topological charge of the polarization vortices is 1 (see Fig. 13 in Appendix E). Besides, when $q_R - q_L$ is nonzero, the topological charge I can be fractional. That is, the odd-fold rotationally symmetric resonators can indeed support the fractional-order polarization singularities. For example, when $M = 7$, $q_R = -1$, and $q_L = 0$, the topological charge I is $-5/2$. This conclusion is illustrated for the D_7 group case (see Figs. 14 and 15 in Appendix E). As a note, the selection of the values of q_L and q_R is closely related to the geometries of resonators. Detailed theory on this aspect will be deliberated in our future work. For the cases where the mirror symmetries are broken, the D_M group reduces to the C_M group. But, even in this case, Eq. (5) is still valid (see proofs in Appendix B).

Lastly, it is noted that polarization singularities can be only properly defined when the out-of-plane component, i.e., the E_z component, is negligible or significantly smaller than the in-plane components. In the current section (e.g., in Fig. 2) and also in the section that follows (e.g., in Fig. 8), the discussions on the E_z component are only included to demonstrate that the symmetries of a scatterer define the topological properties of all three components of the eigen electric fields as a whole. This observation can be useful for constructing vectorial EM field configurations in the near-field regime of the scatterer, e.g., the EM skyrmion in Ref. [47].

3. NUMERICAL VALIDATIONS

In this section, we present two categories of designs to numerically demonstrate the symmetry-based arguments in the previous section. Both categories are designed based on the symmetry-matching conditions in Section 3.B.

A. Designs

The first category is a device [see Figs. 4(a)–4(c)] excited by a one-port feeding network. The first layer of the device is an MPR with the D_8 group symmetries. The MPR is etched on a dielectric plate made of Rogers 4530B (with the relative permittivity 3.48, the loss tangent 0.0037, and the thickness 0.508 mm), which serves as the second layer. The same dielectric plate is used for the third and the fifth layers. The fourth layer is made of metal film and serves as the ground of the device. Two microstrip lines are etched on the lower surface of the fifth layer and the upper surface of the third layer, respectively, and are connected by a "via" through from the third to fifth layer, as shown in Fig. 4(c). Due to the metal ground (the fourth layer), the incident field is dominated by the field radiated by the microstrip line on the upper surface of the third layer, as shown in the top right-hand panel of Fig. 4(c). The third, the fourth, and the fifth layers establish the feeding system. Especially, we have a parameter for tuning the one-port feeding system, i.e., r_{f1}, the length of the microstrip line on the lower surface of the fifth layer.

The second category is a device excited by a two-port feeding network [see Figs. 4(d)–4(f)]. The feeding systems in the third, the fourth, and the fifth layers are redesigned. In detail, two microstrip lines related by a rotation of geometric angle $\Delta\varphi = n\pi/4$ are etched on the upper surface of the third layer and serve as two ports, as shown in Fig. 4(d). The two ports are linked by two vias (marked by "via 1" and "via 2") to a 1-to-2 power divider etched on the lower surface of the fifth layer, as shown in Figs. 4(e) and 4(f). The input power is fed equally to two ports by a power divider. The dynamic phase difference ψ between two ports is realized by a delay line of the divider with the length of Δd in one branch, as shown in Fig. 4(f). Therefore, we have two tunable parameters for tailoring the two-port feeding system, i.e., the geometric angle $\Delta\varphi$ and the length of the delay line Δd [see Fig. 4(f)].

B. Symmetry-Matching Condition

To excite an eigen electric field, the so-called symmetry-matching condition needs to be satisfied (see our previous work [51]).

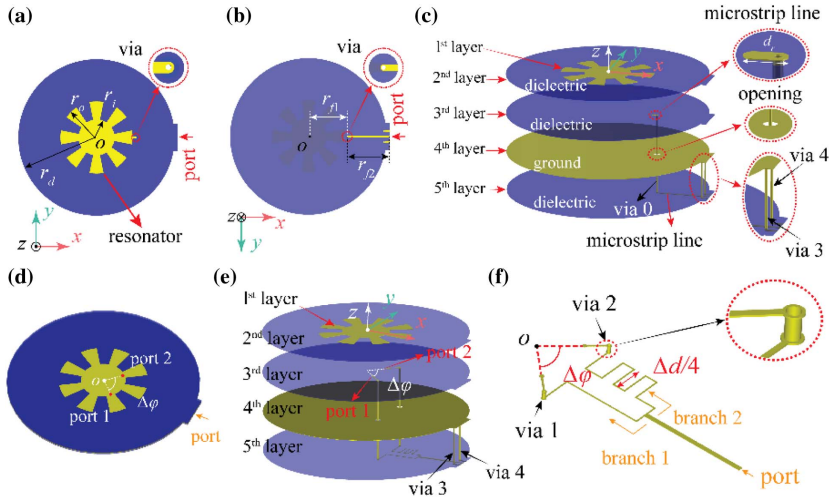

Fig. 4. Illustration of the devices with the one- and the two-port feeding networks. (a), (b), and (c) show the top, the bottom, and the side views of the device with the one-port feeding network. (d) and (e) show the side views of the device with the two-port feeding network. (f) shows the details of the two-port feeding network. In (a)–(c), the adopted parameters are: $r_i = 12$ mm, $r_o = 24$ mm, $r_d = 52$ mm, $r_{f1} = 26$ mm, $r_{f2} = 28$ mm, $d_r = 4$ mm. The width of the microstrip line is 1.1 mm to ensure that the input impedance of the microstrip line is 50 Ω. In (c) and (e), two additional vias marked by "via 3" and "via 4" are to connect the ground of the SMA connector with the fourth layer, i.e., the ground of the microstrip lines.

That is, the incident field must have a nonvanishing projection along the dimension of the irrep that defines the eigen electric field. This argument is due to the orthonormality of the eigen electric fields discussed in Section 2 [48]. In this spirit, for the one-port feeding case, it can be demonstrated that the design given in Figs. 4(a)–4(c) can excite the eigen electric fields belonging to the A_1, the B_1, the E_1, the E_2, and the E_3 irreps (Appendix F.1). For the two-port feeding case, the geometric angle $\Delta\varphi$ and the dynamic phase ψ can be tuned (see our previous work [51] for detailed derivations),

$$\Delta\varphi = \frac{2N_1 + 1}{M - 2j}\pi, \qquad \psi = 2N_2\pi - j\pi\frac{2N_1 + 1}{M - 2j}, \tag{6}$$

so that an eigen electric field belonging to the dimension index by $j = h$ or $j = M - h$ of the E_h irrep can be excited. It is worth noting that Eq. (6) is derived for a resonator with generic D_M group symmetries, where M can be any integer larger than or equal to 2; and N_1 and N_2 are also arbitrary integers. In our design, since the geometric angle $\Delta\varphi$ is assumed to be $n\pi/4$, n is obtained as $\frac{M(2N_1+1)}{2(M-2j)}$.

C. Numerical Results

We numerically simulate the designs with the one- and the two-port feeding networks in CST Microwave Studio (CST). For the one-port case, the reflection coefficient S_{11} in Fig. 5(a) shows that there are five well-separated dips. The excited modes at the dips are marked by $m1$, $m2$, $m3$, $M4$, and $M0$, respectively. From the out-of-plane component, i.e., E_z, at the dips [see Fig. 5(b)], it is observed that the E_z component of the $m1$–$m3$ modes demonstrates the dipole, quadrupole, and hexapole modes, respectively; and the E_z component of the $M4$ and the $M0$ modes does the octopole mode and the zeroth-order mode (or trivial scalar vortex mode with topological

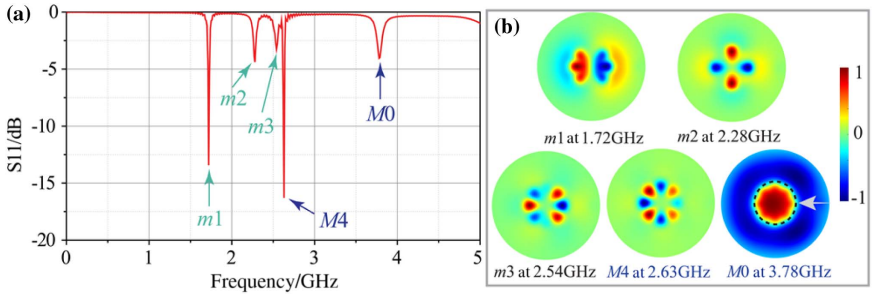

Fig. 5. Illustration of the simulation results for the one-port case in Figs. 4(a)–4(c). The reflection coefficient S_{11} of the MPR is shown in (a). In (a), the dips in the reflection coefficient are marked by $m1$, $m2$, $m3$, $M4$, and $M0$ (from low frequencies to high frequencies), respectively. In (b), the real parts of the E_z component at the five dips are demonstrated. The fields are taken at the $z = 10$ mm cut plane. In the inset of (b), a dashed black circle delineates the profile of the MPR; and a gray arrow points at the position of the via 0 in Fig. 4(c). In (b), the real part of the electric field is normalized to the range between −1 and +1.

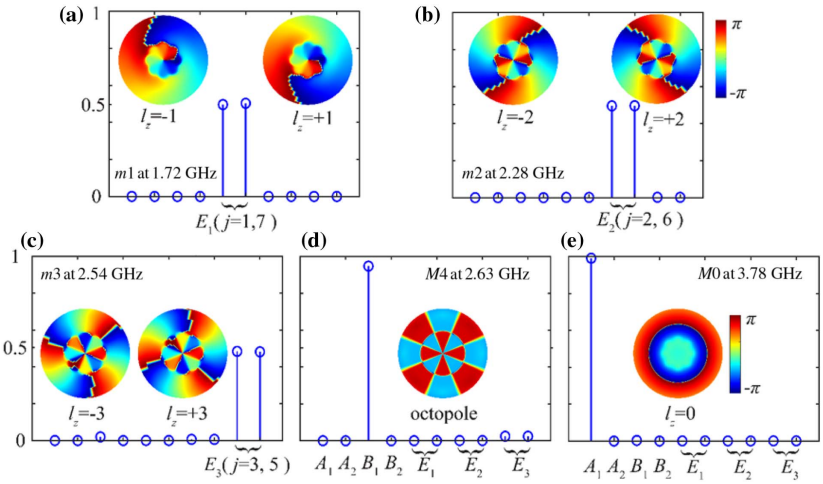

Fig. 6. Projections of the electric fields at the five dips [in Fig. 5(a)] along the dimensions of the irreps of the D_8 group. (a)–(e) correspond to the dips $m1$, $m2$, $m3$, $M4$, and $M0$, respectively. In each subplot, the projections along the dimensions of the irreps (i.e., the vertical axis) are plotted against the dimensions of the irreps (i.e., the horizontal axis). The insets illustrate the phase distributions of the E_z components of the projected fields.

charge of 0), respectively. Then, the E_z component of the modes is projected onto each dimension of the irreps of the D_8 group. It is observed from Fig. 6 that the $m1$, the $m2$, and the $m3$ modes only have nonzero projections along the dimensions indexed by $j = 1, 7$ of the E_1 irrep, the dimensions indexed by $j = 2, 6$ of the E_2 irrep, and the dimensions indexed by $j = 3, 5$ of the E_3 irrep, while the $M4$ and the $M0$ modes only have nonvanishing projections along the B_1 ($j = 4$) and the A_1 ($j = 0$) irreps. Hence, it is said that the $M0$, the $M4$, the $m1$, the $m2$, and the $m3$ modes belong to the A_1, B_1, E_1, E_2, and E_3 irreps. This observation immediately confirms the prediction from the symmetry-matching condition (see Appendix F.1). That is, the designed one-port network excites the eigen electric fields belonging to the dimensions of the A_1, the B_1, the E_1, the E_2, and the E_3 irreps. Further, by comparing Fig. 6 to Fig. 2, it is seen that the projected modes share the same topological features as the corresponding eigen electric fields. For example, for the case $j = 1$, both the projected modes and the eigen electric fields hold a topological charge of −1. For the in-plane components, i.e., $\mathbf{E}_{\parallel}$ (see Fig. 7), we focus on the polarization distributions of the $M4$ and $M0$ modes and delay the discussions on the $m1$, the $m2$, and the $m3$ modes to the two-port case. Since the $M4$ and $M0$ modes belong to the A_1 and B_1 irreps, they should demonstrate the topological charge of +1 and −3 as predicted by Eq. (5) and shown in Fig. 3 (we tailor the geometry of the resonator so that the lowest-order q's, i.e., $q_L = q_R = 0$ are significant). This prediction is readily verified by evaluating the topological charges of the in-plane components of the $M4$ and $M0$ modes (see Fig. 7), respectively. Lastly, by using the symmetry-matching condition as an optimization criterion, we find the optimal length of the microstrip line on the lower surface of the fifth layer, i.e., $r_{f1} = 4$ mm, so that, in contrast to Fig. 5, only the eigen electric field belonging to the A_1 irrep is excited at the $M0$ dip (see the reflection coefficient S_{11} and the electric field in Appendix G).

The one-port feeding network simultaneously excites the two eigen electric fields belonging to the two dimensions of the E_1, the E_2, and the E_3 irreps. To selectively excite the eigen electric field belonging to a specific dimension of the E_1, the E_2, or the E_3 irreps, the two-port feeding network is designed. According to Eq. (6), we tune the geometric angle $\Delta\varphi$, and the dynamic phase ψ (which is thus the length of the delay line Δd) to maximally excite the dimension indexed by $j = 1$ of the E_1 irrep. By the use of Eq. (6), we can obtain $\Delta\varphi = 90°$ and $\psi = -90°$ ($N_1 = 1$, $N_2 = 0$, and $n = 2$). The length of the delay line, i.e., Δd, is calculated to be −27.5 mm so that a −90° phase delay between two ports is achieved at 1.72 GHz, where the linear mode $m1$ appears. This procedure can be applied to other indices j's as well (see the caption of Fig. 8 for the selected parameters of the two-port feeding networks corresponding to different indices j). The simulated out-of-plane and in-plane components, i.e., E_z and $\mathbf{E}_{\parallel}$, are shown in Fig. 8.

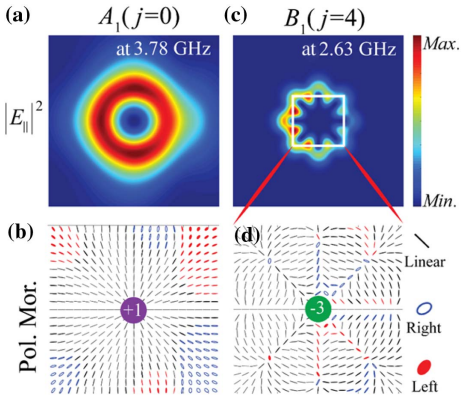

Fig. 7. Illustration of the (a) and (c) intensity and the (b) and (d) polarization distributions of the in-plane components of the excited electric fields at the dips $M4$ and $M0$. The topological charges are marked at the center of (b) and (d).

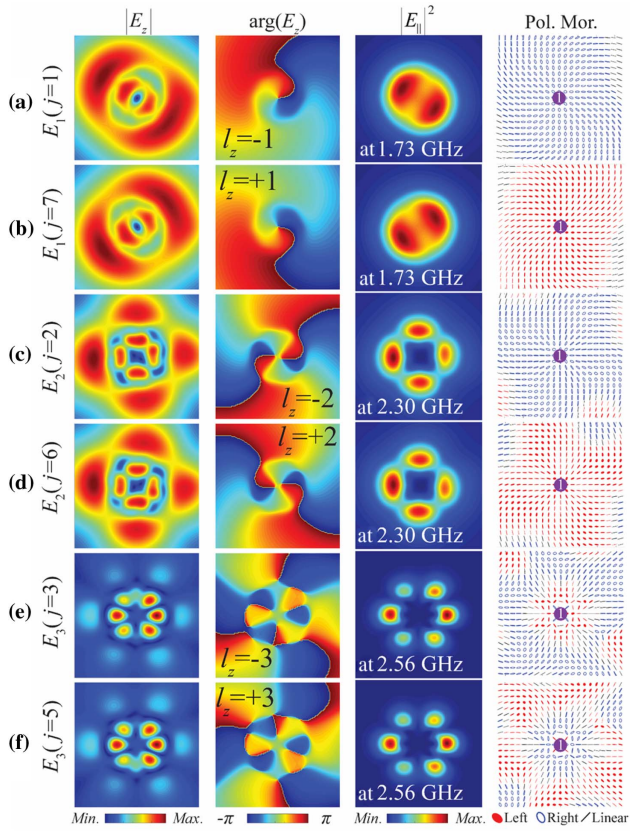

Fig. 8. Illustration of the out-of-plane and the in-plane components, i.e., E_z and $\mathbf{E}_{\|}$ of the excited fields in the two-port feeding designs in Figs. 4(d)–4(f). The fields are taken on a cut plane at $z = 20$ mm. (a) and (b), (c) and (d), (e) and (f) show the E_z and the $\mathbf{E}_{\|}$ belonging to the two dimensions indexed by $j = 1, 7$ of the E_1 irrep, to the two dimensions indexed by $j = 2, 6$ of the E_2 irrep, and to the two dimensions indexed by $j = 3, 5$ of the E_3 irrep, respectively. For the case of $j = 1$ and $j = 7$, the lengths of the delay lines Δd are chosen as –27.5 mm and 27.5 mm, so that –90° and 90° phase delays between two ports are achieved at the targeted frequency 1.72 GHz (in the final simulation, 1.73 GHz). For the cases of $j = 2$ and $j = 6$, the lengths of the delay lines are chosen as –20.8 mm and 20.8 mm, so that –90° and 90° phase delays between two ports are achieved at the targeted frequency 2.28 GHz (in the final simulation, 2.30 GHz). For the case of $j = 3$ and $j = 5$, the lengths of the delay lines Δd are chosen as –18.7 mm and 18.7 mm, so that –90° and 90° phase delays between two ports are achieved at the targeted frequency 2.54 GHz (in the final simulation, 2.56 GHz).

For the out-of-plane component, i.e., E_z, it can be observed that the scalar vortex modes with topological charges of ∓ 1, ∓ 2, and ∓ 3 (corresponding to the dimensions of the irreps indexed by $j = 1, 7$, $j = 2, 6$, and $j = 3, 5$) are excited by the designed two-port feeding networks. For the in-plane components, i.e., $\mathbf{E}_{\|}$, the polarization distributions indexed by $j = 1, 2, 3$ and $j = 7, 6, 5$ exhibit right-handed and left-handed elliptical polarizations and hold C-point singularities with topological charges $+1$ (see the E_L, the E_R, and the Stokes fields in Appendix H). The resonant frequencies in Fig. 8 are retrieved from the simulated reflection coefficient S_{11} of each two-port feeding network (see Appendix I). Comparing the frequencies in Fig. 8 to the ones in Fig. 5, it can be observed that there are small frequency shifts. The differences are due to the feeding networks: that is, in Figs. 5 and 8, one-port and two-port feeding networks are used. Finally, it is noted that for the A_2 and B_2 irreps, the corresponding eigen electric fields cannot be excited by the designed one- or two-port feeding system. More complex feeding systems are needed (see discussions in Appendix F.2). As a caveat, it is noted that Fig. 8 focuses on the near-field regime of the resonator, where both the out-of-plane and the in-plane components of electric fields are significant. However, this is only to validate the theoretical arguments in Section 2, i.e., Eqs. (1) and (5), and to demonstrate that the symmetries of the resonator indeed define the topological singularities in all three field components. To be in line with the definition of in-plane polarization singularities (see the end of Section 2), we plot the electric field corresponding to the $j = 7$ case on different cuts above the resonator in Appendix J. There, the out-of-plane component is weak enough so that in-plane polarization singularities can be properly defined.

Last but not least, it is worth mentioning that, since the one- and the two-port feeding networks do not hold the D_8 group symmetries of the resonator, adding them as excitations indeed breaks the symmetries of the resonator. This results in a splitting of the C-type polarization singularities in Fig. 8 (see details in Appendix H). Especially, for the two-port feeding network case, it has to be emphasized that the design rules in Eq. (6) aim to maximally but not exclusively excite the eigen electric fields belonging to a specific dimension of an E_j irrep. That is, the feeding network can still excite eigen electric fields belonging to other dimensions of the irreps but only in a parasitic manner. To exclusively excite a specific dimension, a feeding network that fully matches the symmetries of the resonator is needed. This feeding network requires 16 ports and is envisaged in Appendix F.2.

4. CONCLUSIONS

In conclusion, we systematically investigate the relation between the symmetries of an EM resonator and the topological features of the in-plane polarization distributions supported by the resonator. The relation is consolidated: 1) the morphologies of polarization distributions are categorized by the irreps determined by the symmetries of the resonator, and 2) the topological charges of the polarization distributions are directly linked with the irreps through Eqs. (5) and (6). Although our discussions focus on the relation between the in-plane electric fields supported by the resonator, and the discrete rotation and reflection symmetries of a planar microwave resonator, the same methodology can be applied to the discussions on the vector fields defined on other spaces, e.g., the momentum space, and the other types of symmetries, e.g., the translational symmetries in a lattice. This line of reasoning can be very helpful in searching for the symmetry origins of many photonic effects.

APPENDIX A: SYMMETRIES

1. C_M Group and D_M Group

In this work, we consider a planar metal resonator (we assume that the planar resonator is positioned at $z = 0$ in the

Table 1. Diagonal Elements of the Irreps of the C_M Group (M Is an Odd Integer)

	j	r^m
A	$j=0$	$(\varepsilon^j)^m$
E_h $[h=1,\cdots,(M-1)/2]$	$j=h$	$(\varepsilon^j)^m$
	$j=M-h$	$(\varepsilon^j)^m$

Table 2. Diagonal Elements of the Irreps of the C_M Group (M Is an Even Integer)

	j	r^m
A	$j=0$	$(\varepsilon^j)^m$
B	$j=M/2$	$(\varepsilon^j)^m$
E_h $[h=1,\cdots,M/2-1]$	$j=h$	$(\varepsilon^j)^m$
	$j=M-h$	$(\varepsilon^j)^m$

x-y plane). Although the geometry of the resonator can be arbitrary, it always holds M-fold rotational and M-fold reflection symmetries. The symmetries form the D_M group. The generators of the group [48] are r and s. r is a rotation of an angle $\theta_0=2\pi/M$ with respect to the z axis, and s is a reflection that makes an angle $\theta_0/2$ with respect to the x axis [see the rotation, the reflection, and the coordinate system in Fig. 1(b) in the main text]. The elements of the group are a set of rotations $\{1, r, \cdots, r^{M-1}\}$ and a set of reflections $\{s, sr, \cdots, sr^{M-1}\}$. In the set of rotations, 1 is the identity operation that keeps the resonator unchanged. Especially, the set of the rotations forms an important subgroup, i.e., the C_M group and the D_M group.

2. Irrep of the C_M Group and the D_M Group

Lying at the core of the group representation theory are the irreps. The irreps are essentially matrices [48]. In this work, we mark an irrep with the Greek letter Γ. In the following, we specifically focus on the irreps of the C_M and the D_M groups.

First, we look at the irreps of the C_M group and consider two cases: the odd M case and the even M case.

For an odd M, A labels a 1D irrep (that is, a scalar that is a 1D matrix), while E_h (h is an integer spanning from 1 to $(M-1)/2$) labels a 2D irrep (that is, two dimensional matrices).

For an even M, A and B label 1D irreps, while E_h (h is an integer spanning from 1 to $M/2-1$) labels a 2D irrep.

The diagonal elements of the irreps are listed in Tables 1 and 2. It can be seen from the tables that the diagonal elements of the irreps hold a general form, i.e., $(\varepsilon^j)^m$. Here, ε is equal to $e^{i\theta_0}$, with θ_0 being defined as $2\pi/M$. m is an integer spanning from 0 to $M-1$ so that all the rotation operations are covered. And j is an integer that gives an index to each dimension of the irreps.

Second, we turn our focus to the D_M group and again consider two cases: the odd M case and the even M case. The diagonal elements of the irreps of the D_M group are shown in Tables 3 and 4.

For an odd M, A_1, A_2 label two 1D irreps (that is, 1D matrices), while E_h [h is an integer spanning from 1 to $(M-1)/2$]

Table 3. Diagonal Elements of the Irreps of the D_M Group (M Is an Odd Integer)

	j	r^m	sr^m
A_1	$j=0$	$(\varepsilon^j)^m$	$(\varepsilon^j)^m$
A_2		$(\varepsilon^j)^m$	$-(\varepsilon^j)^m$
E_h $[h=1,\cdots,(M-1)/2]$	$j=h$	$(\varepsilon^j)^m$	0
	$j=M-h$	$(\varepsilon^j)^m$	0

Table 4. Diagonal Elements of the Irreps of the D_M Group (M Is an Even Integer)

	j	r^m	sr^m
A_1	$j=0$	$(\varepsilon^j)^m$	$(\varepsilon^j)^m$
A_2		$(\varepsilon^j)^m$	$-(\varepsilon^j)^m$
B_1	$j=M/2$	$(\varepsilon^j)^m$	$(\varepsilon^j)^m$
B_2		$(\varepsilon^j)^m$	$-(\varepsilon^j)^m$
E_h $[h=1,\cdots,M/2-1]$	$j=h$	$(\varepsilon^j)^m$	0
	$j=M-h$	$(\varepsilon^j)^m$	0

labels 2D irreps (that is, two dimensional matrices). It can be proven [48] that: 1) the A_1 and the A_2 irreps are originated from the A irrep, and hence they inherit the index $j=0$ from the A irrep of the C_M group; and 2) the E_h irrep of the D_M group is the same as the E_h of the C_M group and thus the indices stay the same.

For an even M, A_1, A_2, B_1, B_2 label four 1D irreps, while E_h (h is an integer spanning from 1 to $M/2-1$) labels 2D irreps. The A_1 and the A_2 irreps, and the B_1 and the B_2 irreps are indexed by $j=0$ and $j=M/2$, respectively, because they stem from the A and the B irreps of the C_M group. The E_h irreps and their indices are again the same as the ones of the C_M group.

3. Concept of Projection Operators and Basis Functions

It is remembered that the irreps are essentially matrices and marked by the Greek letter Γ in this work. For the ith dimension (or the ith row) of an irrep Γ, a projection operator can be defined,

$$\mathcal{P}_i^{\Gamma}=\frac{d(\Gamma)}{N}\sum_R \Gamma_{ii}^*(R)\cdot P_R. \tag{A1}$$

Take the irreps of the D_M group as an example. On the left-hand side of Eq. (A1), the superscript Γ of the projection operator can be A_1, A_2, and E_h for the odd M case, and can be A_1, A_2, B_1, B_2, and E_h for the even M case. The subscript i of the projection operator is the dimension (or row) index. On the right-hand side of Eq. (A1), N is the number of symmetries in the group. For the D_M group, N is equal to $2M$. $d(\Gamma)$ is the dimension of the irrep Γ. The summation is done with respect to R, that is, all the symmetry operations in the group. For each symmetry operation R, there is a matrix $\Gamma(R)$ and $\Gamma_{ii}(R)$ is the diagonal element on the ith dimension (or row/column) of the matrix. P_R is the transformation operator [48,49],

$$P_R f(\mathbf{r})=f(\mathbf{R}^{-1}\cdot\mathbf{r}),\qquad P_R\mathbf{f}(\mathbf{r})=\mathbf{R}\cdot\mathbf{f}(\mathbf{R}^{-1}\cdot\mathbf{r}). \tag{A2}$$

Equation (A2) defines the transformation rule when applying the transformation operator to a scalar and a vector function.

Applying the projection operator in Eq. (A1) to an arbitrary function leads to

$$\mathcal{P}_i^{\Gamma} f(\mathbf{r}) = f_i^{\Gamma}(\mathbf{r}), \qquad \mathcal{P}_i^{\Gamma}\mathbf{f}(\mathbf{r}) = \mathbf{f}_i^{\Gamma}(\mathbf{r}). \tag{A3}$$

In Eq. (A3), the projection operator is applied to a scalar function and a vector function, respectively. Since the projection operator is defined for the ith dimension (or row) of the irrep Γ, the projected functions f_Γ^i and $\mathbf{f}_\Gamma^i$ are said to belong to the ith dimension (or row) of the irrep Γ. It can be proven [48] that the projected functions belonging to different rows of an irrep or belonging to different irreps are orthogonal and form a basis for expanding a generic function. In this sense, the projected functions are also called "basis functions" [49]. Notably, the effect of a transformation operator on a basis function belonging to the ith dimension of an irrep Γ is (see (3–23) in Ref. [49]),

$$P_R f_i^{\Gamma}(\mathbf{r}) = \Gamma_{ii}(R) f_i^{\Gamma}(\mathbf{r}), \qquad P_R \mathbf{f}_i^{\Gamma}(\mathbf{r}) = \Gamma_{ii}(R)\mathbf{f}_i^{\Gamma}(\mathbf{r}). \tag{A4}$$

As a note, as seen from Tables 3 and 4, for an E_h irrep, the diagonal elements of the irrep are zero for reflection symmetry operations. This indicates that the reflection symmetries play **no role** in the construction of the projection operators corresponding to the two dimensions (the two rows) of the irrep. As a result, for a specific dimension of an E_h irrep, the projection operator and the basis function for the D_M group are the same as the ones for the C_M group.

APPENDIX B: BASIS FUNCTIONS FOR THE C_M GROUP AND THE D_M GROUP

1. C_M Group

First, we focus on the C_M group. We remember that, on the one hand, all the dimensions (rows) of the irreps of the C_M group (see Section 2.A in the main text and Tables 1 and 2 in Appendix A) are indexed by unique integers, i.e., j's; on the other hand, by Eqs. (A1) and (A3), all the dimensions (rows) of the irreps of the C_M group uniquely define their corresponding projection operators and basis functions. Therefore, the projection operators and basis functions can be labeled by the same integers. Further, since j consecutively spans 0 to $M-1$, we can call the projection operator and the basis function labeled by a given integer j as the jth operator and the jth basis function.

Then, we consider the jth basis function. Here, the jth basis function, i.e., $\mathbf{f}_j(\mathbf{r})$, is a vector function where $\mathbf{r}$ is a point in the x-y plane and has two components. In the following, we consider the left and the right circular bases,

$$\hat{L} = \frac{1}{\sqrt{2}}\begin{pmatrix} 1 \\ +i \end{pmatrix}, \qquad \hat{R} = \frac{1}{\sqrt{2}}\begin{pmatrix} 1 \\ -i \end{pmatrix}. \tag{B1}$$

The jth basis function can be expanded as

$$\mathbf{f}_j(\mathbf{r}) = f_j^L(\mathbf{r})\hat{L} + f_j^R(\mathbf{r})\hat{R}. \tag{B2}$$

In the above equation, $f_j^L(\mathbf{r})$ and $f_j^R(\mathbf{r})$ are the left and the right circular components of the basis function. We apply a rotation r, which is a rotation around the z axis by $\theta_0 = 2\pi/M$, to the jth basis function. On the one hand, Eq. (A2) leads to

$$\begin{aligned} P_R\mathbf{f}_j(\mathbf{r}) &= \mathbf{R}\cdot\mathbf{f}_j(\mathbf{R}^{-1}\cdot\mathbf{r}) \\ &= \mathbf{R}\cdot[f_j^L(\mathbf{R}^{-1}\cdot\mathbf{r})\hat{L} + f_j^R(\mathbf{R}^{-1}\cdot\mathbf{r})\hat{R}]. \end{aligned} \tag{B3}$$

By using the polar coordinate, i.e., $\mathbf{r} = (\rho, \theta)$ and noting that

$$\mathbf{R}\cdot\hat{L} = \hat{L}e^{-i\theta_0}, \qquad \mathbf{R}\cdot\hat{R} = \hat{R}e^{i\theta_0}, \tag{B4}$$

Equation (B3) becomes

$$P_R\mathbf{f}_j(\mathbf{r}) = f_j^L(\rho, \theta-\theta_0)e^{-i\theta_0}\hat{L} + f_j^R(\rho,\theta-\theta_0)e^{i\theta_0}\hat{R}. \tag{B5}$$

On the other hand, Eq. (A4) leads to

$$P_R\mathbf{f}_j(\mathbf{r}) = e^{ij\theta_0}[f_j^L(\rho,\theta)\hat{L} + f_j^R(\rho,\theta)\hat{R}]. \tag{B6}$$

We equate Eq. (B5) with Eq. (B6),

$$f_j^L(\rho,\theta-\theta_0) = e^{i(j+1)\theta_0} f_j^L(\rho,\theta), \tag{B7}$$

$$f_j^R(\rho,\theta-\theta_0) = e^{i(j-1)\theta_0} f_j^R(\rho,\theta). \tag{B8}$$

Further, we note that Eqs. (B7) and (B8) are invariant by multiplying 1 on both sides of the equations,

$$f_j^L(\rho,\theta-\theta_0) = e^{i(j+1+q_L M)\theta_0} f_j^L(\rho,\theta), \tag{B9}$$

$$f_j^R(\rho,\theta-\theta_0) = e^{i(j-1+q_R M)\theta_0} f_j^R(\rho,\theta). \tag{B10}$$

In Eqs. (B9) and (B10), we have used $(e^{iM\theta_0})^{q_L} = (e^{iM\theta_0})^{q_R} = 1$ where q_L and q_R are integers. More importantly, the multiplication of 1 on both sides is more than a mathematical manipulation. Physically, Eqs. (B9) and (B10) are closely related to the fact that multiple full-phase (from 0 to 2π) variations can be accommodated within a period θ_0. An ansatz for $f_j^L(\mathbf{r})$ is

$$f_j^L(\rho,\theta) = u_j^L(\rho,\theta)e^{-i(j+1+q_L M)\theta}. \tag{B11}$$

In the above equation, u_j^L is a periodic function of the azimuthal angle θ. This assumed form can be readily verified by substituting Eq. (B11) in the left-hand side of Eq. (B7),

$$\begin{aligned} f_j^L(\rho,\theta-\theta_0) &= u_j^L(\rho,\theta-\theta_0)e^{-i(j+1+q_L M)(\theta-\theta_0)} \\ &= e^{i(j+1+q_L M)\theta_0}\cdot u_j^L(\rho,\theta)e^{-i(j+1+q_L M)\theta} \\ &= e^{i(j+1+q_L M)\theta_0}\cdot f_j^L(\rho,\theta). \end{aligned} \tag{B12}$$

The above recovers the relation in Eq. (B9). Similarly, an ansatz for $f_j^R(\mathbf{r})$ is

$$f_j^R(\rho,\theta) = u_j^R(\rho,\theta)e^{-i(j-1+q_R M)\theta}. \tag{B13}$$

Again, u_j^R is a periodic function of the azimuthal angle θ. Examining Eqs. (B11) and (B12) readily leads to the conclusion that both the left component and the right component of the jth basis function are scalar vortices. The topological charges of the vortices are

$$l_L = -(j+1+q_L M), \qquad l_R = -(j-1+q_R M). \tag{B14}$$

Thus, the topological charge of a polarization singularity in the jth basis function is

$$I = \frac{1}{2}(l_R - l_L) = 1 + (q_L - q_R)\frac{M}{2}. \tag{B15}$$

To be complete, the jth basis function in Eq. (B2) becomes

$$\mathbf{f}_j(\mathbf{r}) = u_j^L(\rho,\theta)e^{-i(j+1+q_LM)\theta}\hat{L} + u_j^R(\rho,\theta)e^{-i(j-1+q_RM)\theta}\hat{R}. \tag{B16}$$

2. D_M Group

Second, we look at the D_M group. As discussed at the end of Appendix A, since for a specific dimension (row) of the E_h irrep, the basis function of the D_M group is the same as the one of the C_M group; the conclusions for the basis functions corresponding to the E_h irreps of the C_M group remain the same for the E_h irreps of the D_M group. We note that, for the D_M group, these unchanged basis functions are labeled by 1) when M is odd, j spanning 1 to $M-1$; and 2) when M is even, j spanning 1 to $M/2-1$ and $M/2+1$ to $M-1$. Hence, we only need to consider: 1) when M is odd or even, the $j=0$ case (which labels the A_1 irrep and the A_2 irrep of the D_M group); and 2) when M is even, the $j=M/2$ case (which labels the B_1 irrep and the B_2 irrep of the D_M group).

For the A_1 irrep and the A_2 irrep, the basis functions can be obtained as

$$\mathbf{f}_0^{A_1}(\mathbf{r}) = \mathbf{f}_0(\mathbf{r}) + P_s\mathbf{f}_0(\mathbf{r}), \quad \mathbf{f}_0^{A_2}(\mathbf{r}) = \mathbf{f}_0(\mathbf{r}) - P_s\mathbf{f}_0(\mathbf{r}). \tag{B17}$$

In Eq. (B17), the subscript of $\mathbf{f}_0^{A_1}(\mathbf{r})$ and $\mathbf{f}_0^{A_2}(\mathbf{r})$ emphasizes that we are considering the case $j=0$, and their superscripts A_1 and A_2 mark that $\mathbf{f}_0^{A_1}(\mathbf{r})$ and $\mathbf{f}_0^{A_2}(\mathbf{r})$ are the basis functions of the A_1 and the A_2 irreps. Further, $\mathbf{f}_0$ is the basis function in Eq. (B16) when $j=0$. Lastly, P_s is the transformation operator [defined in Eq. (A2)] of the reflection operation s (which is defined at the very beginning of Appendix A). s defines a reflection matrix,

$$\mathbf{s} = \mathbf{s}^{-1} = \begin{pmatrix} \cos\theta_0 & \sin\theta_0 \\ \sin\theta_0 & -\cos\theta_0 \end{pmatrix}. \tag{B18}$$

We note the following identities:

$$\mathbf{s}^{-1}\cdot\mathbf{r} = \begin{pmatrix} \cos\theta_0 & \sin\theta_0 \\ \sin\theta_0 & -\cos\theta_0 \end{pmatrix}\cdot\begin{pmatrix} \rho\cos\theta \\ \rho\sin\theta \end{pmatrix} = \begin{pmatrix} \rho\cos(\theta_0-\theta) \\ \rho\sin(\theta_0-\theta) \end{pmatrix}, \tag{B19}$$

$$\mathbf{s}\cdot\hat{L} = \begin{pmatrix} \cos\theta_0 & \sin\theta_0 \\ \sin\theta_0 & -\cos\theta_0 \end{pmatrix}\cdot\frac{1}{\sqrt{2}}\begin{pmatrix} 1 \\ +i \end{pmatrix} = \frac{1}{\sqrt{2}}\begin{pmatrix} 1 \\ -i \end{pmatrix}e^{i\theta_0} = \hat{R}e^{i\theta_0}, \tag{B20}$$

$$\mathbf{s}\cdot\hat{R} = \begin{pmatrix} \cos\theta_0 & \sin\theta_0 \\ \sin\theta_0 & -\cos\theta_0 \end{pmatrix}\cdot\frac{1}{\sqrt{2}}\begin{pmatrix} 1 \\ -i \end{pmatrix} = \frac{1}{\sqrt{2}}\begin{pmatrix} 1 \\ i \end{pmatrix}e^{-i\theta_0} = \hat{L}e^{-i\theta_0}. \tag{B21}$$

Therefore, $P_s\mathbf{f}_0(\mathbf{r})$ in Eq. (B17) reads

$$\begin{aligned} P_s\mathbf{f}_0(\mathbf{r}) &= u_0^L(\rho,\theta_0-\theta)e^{-i(q_LM+1)(\theta_0-\theta)}\hat{R}e^{i\theta_0} \\ &\quad + u_0^R(\rho,\theta_0-\theta)e^{-i(q_RM-1)(\theta_0-\theta)}\hat{L}e^{-i\theta_0} \\ &= u_0^L(\rho,-\theta)e^{+i(q_LM+1)\theta}\hat{R} + u_0^R(\rho,-\theta)e^{i(q_RM-1)\theta}\hat{L}. \end{aligned} \tag{B22}$$

Then, the basis functions in Eq. (B17) are

$$\begin{aligned} \mathbf{f}_0^{A_1}(\mathbf{r}) &= [u_0^L(\rho,\theta)e^{-i(q_LM+1)\theta} + u_0^R(\rho,-\theta)e^{i(q_RM-1)\theta}]\hat{L} \\ &\quad + [u_0^R(\rho,\theta)e^{-i(q_RM-1)\theta} + u_0^L(\rho,-\theta)e^{+i(q_LM+1)\theta}]\hat{R}, \end{aligned} \tag{B23}$$

$$\begin{aligned} \mathbf{f}_0^{A_2}(\mathbf{r}) &= [u_0^L(\rho,\theta)e^{-i(q_LM+1)\theta} - u_0^R(\rho,-\theta)e^{i(q_RM-1)\theta}]\hat{L} \\ &\quad + [u_0^R(\rho,\theta)e^{-i(q_RM-1)\theta} - u_0^L(\rho,-\theta)e^{+i(q_LM+1)\theta}]\hat{R}. \end{aligned} \tag{B24}$$

Since q_L and q_R are arbitrary integers, for example, we can choose $q_L = -q_R = q$,

$$\begin{aligned} \mathbf{f}_0^{A_1}(\mathbf{r}) &= [u_0^L(\rho,\theta) + u_0^R(\rho,-\theta)]e^{-i(qM+1)\theta}\hat{L} \\ &\quad + [u_0^R(\rho,\theta) + u_0^L(\rho,-\theta)]e^{+i(qM+1)\theta}\hat{R}, \end{aligned} \tag{B25}$$

$$\begin{aligned} \mathbf{f}_0^{A_2}(\mathbf{r}) &= [u_0^L(\rho,\theta) - u_0^R(\rho,-\theta)]e^{-i(qM+1)\theta}\hat{L} \\ &\quad + [u_0^R(\rho,\theta) - u_0^L(\rho,-\theta)]e^{+i(qM+1)\theta}\hat{R}. \end{aligned} \tag{B26}$$

Based on Eqs. (B25) and (B26), we can identify the topological charges of the scalar vortices in the left circular and the right circular components of the A_1 irrep and the A_2 irrep,

$$l_L = -(1+qM), \qquad l_R = +(1+qM). \tag{B27}$$

Equation (B27) is completely in line with Eq. (B14) for the C_M group case.

For the B_1 and the B_2 irreps, the basis functions can be obtained as

$$\mathbf{f}_4^{B_1}(\mathbf{r}) = \mathbf{f}_4(\mathbf{r}) + P_s\mathbf{f}_4(\mathbf{r}), \qquad \mathbf{f}_4^{B_2}(\mathbf{r}) = \mathbf{f}_4(\mathbf{r}) - P_s\mathbf{f}_4(\mathbf{r}). \tag{B28}$$

In Eq. (B28), the subscript of $\mathbf{f}_4^{B_1}(\mathbf{r})$ and $\mathbf{f}_4^{B_2}(\mathbf{r})$ emphasizes that we are considering the case $j=4$, and their superscripts B_1 and B_2 mark that $\mathbf{f}_0^{B_1}(\mathbf{r})$ and $\mathbf{f}_0^{B_2}(\mathbf{r})$ are the basis functions of the B_1 and the B_2 irreps. Further, $\mathbf{f}_4$ is the basis function in Eq. (B16) when $j=4$. The procedures are the same as the ones for the A_1 and the A_2 irreps and will not be repeated here. The result is that the topological charges of the scalar vortices in the left circular and the right circular components of the B_1 irrep and the B_2 irrep,

$$l_L = -\left(\frac{M}{2}+1+qM\right), \qquad l_R = -\left(\frac{M}{2}-1+qM\right). \tag{B29}$$

Again, Eq. (B29) is completely in line with Eq. (B14) for the C_M group case.

In conclusion, based on the above analysis, the relation in Eq. (B14) is still valid for the D_M group case. Therefore, Eq. (B15) is a general formula for both the C_M group and the D_M group cases.

APPENDIX C: SYNTHESIZED STOKES FIELDS

In the following, we evaluate the topological charges of polarization singularities based on the Stokes field. The Stokes parameters are defined as [17,52]

$$S_0 = I_x + I_y = |E_x|^2 + |E_y|^2, \tag{C1}$$

$$S_1 = I_x - I_y = |E_x|^2 - |E_y|^2, \tag{C2}$$

$$S_2 = I_{45^\circ} + I_{-45^\circ} = 2\,\mathrm{Re}(E_x^* \cdot E_y), \tag{C3}$$

$$S_3 = I_{\mathrm{LCP}} - I_{\mathrm{RCP}} = 2\,\mathrm{Im}(E_x^* \cdot E_y). \tag{C4}$$

In the above equations, I_x and I_y, I_{45° and I_{-45°, and I_{LCP} and I_{RCP} are the intensities of the components of a polarization state along x, y bases, 45°, −45° bases, and circular bases, respectively. Based on Eqs. (C2) and (C3), a Stokes field, i.e., S_{12}, is synthesized as

$$S_{12} = S_1 + iS_2 = |S_{12}|e^{i\phi_{12}}. \tag{C5}$$

The Stokes index is related to the phase of the Stokes field in Eq. (C5),

$$\sigma_{12} = \frac{1}{2\pi}\oint \nabla\phi_{12} \cdot \mathrm{d}\mathbf{s}. \tag{C6}$$

The topological charge of a polarization singularity (a C point or a V point) can be obtained from the Stokes index in Eq. (C6), i.e.,

$$I_C \quad \text{or} \quad I_V = \frac{\sigma_{12}}{2}. \tag{C7}$$

As an example, the magnitude and the phase of the synthesized Stokes fields are plotted in Fig. 9 for the in-plane components of the eigen electric fields belonging to the dimensions of the irreps of the D_8 group (see Fig. 3 in the main text). The Stokes index and the topological charge can be directly read out from Fig. 9.

We also apply the normalized Stokes field S_3/S_0 to validate the C points in Fig. 3. Different values of the S_3/S_0 reflect different local polarization states formed: when $S_3/S_0 = 1$, the polarization state is left circularly polarized; when $0 < S_3/S_0 < 1$, the polarization state is left elliptically polarized; when $S_3/S_0 = 0$, the polarization state is linearly polarized; when

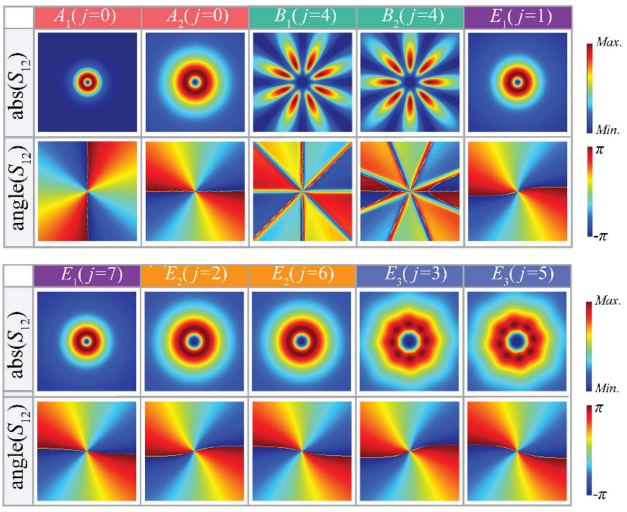

Fig. 9. Illustration of the magnitude distribution and the phase distribution of the Stokes field S_{12} (corresponding to Fig. 3 in the main text).

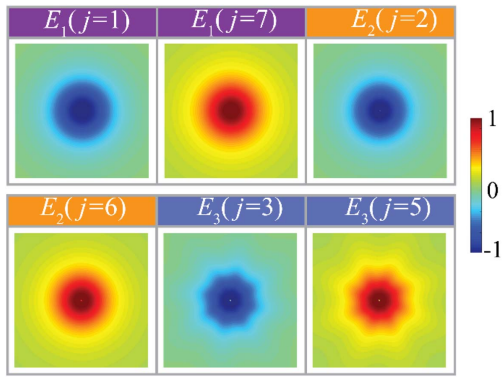

Fig. 10. Illustration of the normalized Stokes parameters S_3/S_0 (corresponding to Fig. 3 in the main text).

$-1 < S_3/S_0 < 0$, the polarization state is right elliptically polarized; and when $S_3/S_0 = -1$, the polarization state is right circularly polarized [52].

Figure 10 demonstrates that the C-type polarization singularities with different handedness are indeed formed in the in-plane electric fields belonging to the E_1, the E_2, and the E_3 irreps (see Fig. 3 in the main text). To be specific, take

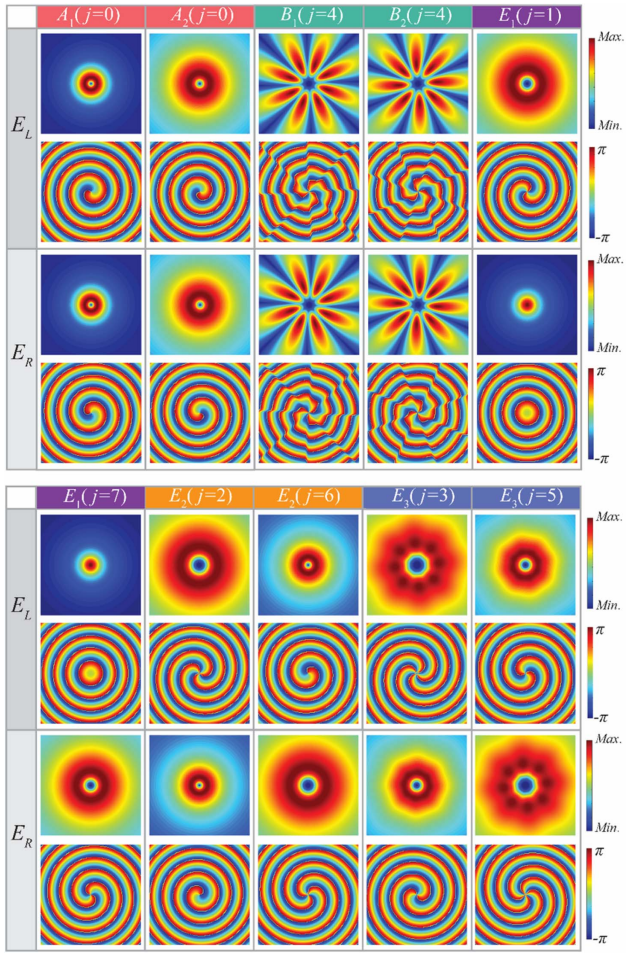

Fig. 11. Illustration of the magnitude and phase distributions of the E_L and the E_R components of the in-plane eigen electric fields for all the irreps of the D_8 group.

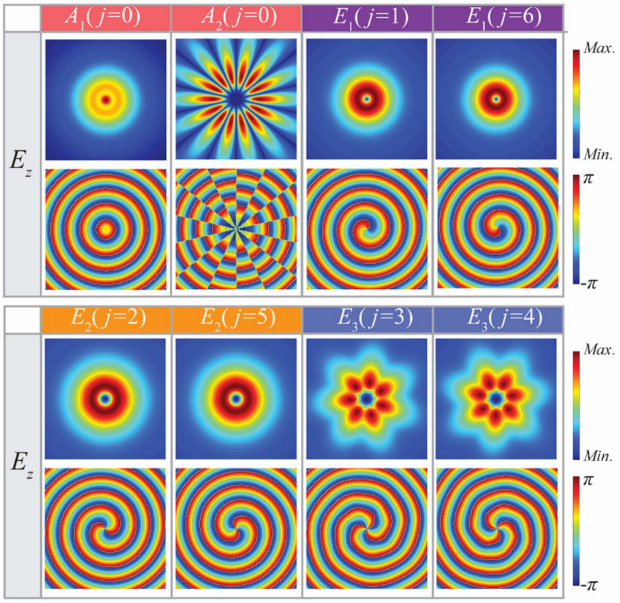

Fig. 12. Illustration of the magnitude and phase distributions of the E_z component of the eigen electric fields corresponding to the irreps of the D_7 group.

the upper-left subplot in Fig. 10 as an example. S_3/S_0 varies from 0 at the boundary to −1 at the center, which suggests a left-handed C point is formed. This result is consistent with the polarization ellipse plot in the main text (see the right-most subplot in the upper panel of Fig. 3). This conclusion applies to the other subplots in Fig. 10 as well. However, it is worth noting that in Fig. 10 there are singular points at the center of the S_3/S_0 plot for the E_2 and the E_3 irreps. This is due to the fact that the null intensities of the in-plane electric fields appear at the central points.

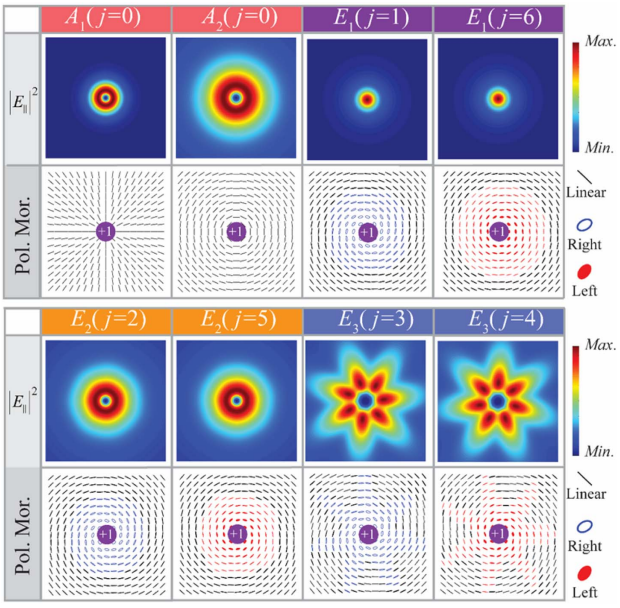

Fig. 13. Illustration of the intensity and the polarization distributions of the in-plane components of the eigen electric fields corresponding to the irreps of the D_7 group.

APPENDIX D: D_8 GROUP CASE

In this appendix, we illustrate the left and the right components of the in-plane eigen electric fields for the D_8 group in Fig. 11.

APPENDIX E: D_7 GROUP CASE

In this appendix, first, in parallel with Figs. 2 and 3 in the main text, we demonstrate the eigen electric fields for the D_7 group case in Fig. 12 (the E_z component) and Fig. 13 (the in-plane components). Here, we tailor the geometry of the resonator in such a way that q_L and q_R are zero and thus according to Eq. (5) in the main text, the topological charge of the polarization singularity is 1. Second, we design another resonator, so that $q_L = 0$ and $q_R = -1$ are selected. Again, by Eq. (5) in the main text, a topological charge $I = -5/2$ can be realized (see Figs. 14 and 15).

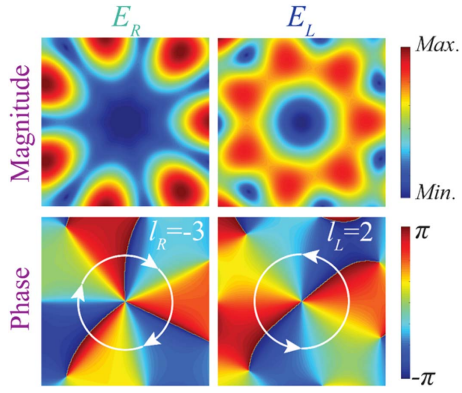

Fig. 14. Illustration of the magnitude and the phase distributions of two circular components of the in-plane eigen electric field corresponding to the second dimension (row) of the E_3 irrep (marked by $j = 4$) of the D_7 group. It can be observed that the E_R and the E_L exhibit two scalar vortex modes with topological charge of −3 and 2, respectively.

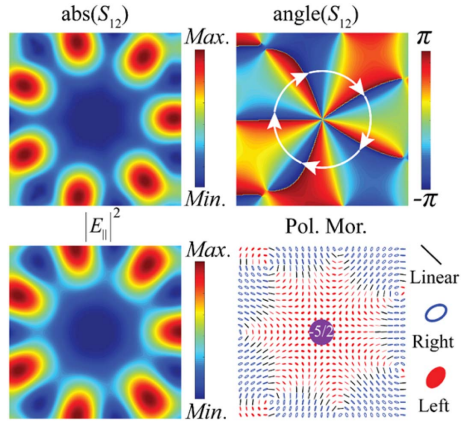

Fig. 15. Illustration of the magnitude and the phase distributions of the Stokes field S_{12}, and the intensity and the polarization distributions of the in-plane eigen electric field corresponding to the second dimension (row) of the E_3 irrep (marked by $j = 4$) of the D_7 group. It can be observed that the Stokes field S_{12} exhibits a scalar vortex with a topological charge of −5, and thus the in-plane eigen electric field carries a polarization singularity with a topological charge of −5/2.

APPENDIX F: SYMMETRY-MATCHING CONDITION

1. One-Port Feeding Network

Since the length of the microstrip line (which is 4 mm) on the third layer is significantly smaller than the smallest operating wavelength (which is around 80 mm) of the resonator, the microstrip line can be seen as an electric dipole. Then, the electric field radiated by such a dipole is evaluated and projected to the irreps of the D_8 group (see Fig. 16). It is readily found that the incident field generated by the microstrip line has nonvanishing projections along the A_1, the B_1, the E_1, the E_2, and the E_3 irreps. Thus, the one-port feeding network can excite the currents, and their scattered fields belong to these irreps.

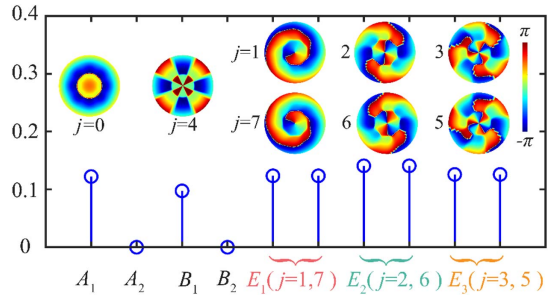

Fig. 16. Projections of the electric field radiated by the electric dipole oscillating at 1.72 GHz along the dimensions of the irreps of the D_8 group. The projections along the dimensions of the irreps (i.e., the vertical axis) are plotted against the dimensions of the irreps (i.e., the horizontal axis). The insets illustrate the phase distributions of the E_z components of the projected fields. Notably, here for the sake of compactness, we only demonstrate the projected fields at the first resonant point (i.e., 1.72 GHz). For other resonant frequency points (e.g., 2.28, 2.54, 2.63, and 3.78 GHz), similar behaviors can be observed as well.

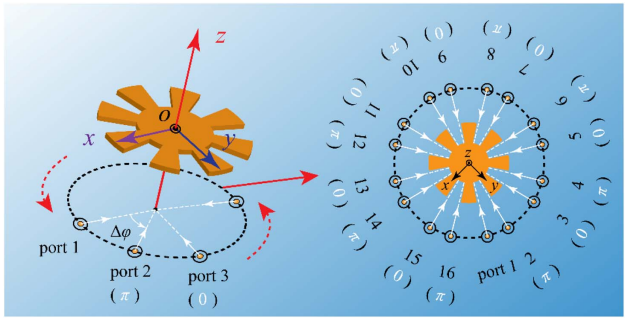

Fig. 17. Illustration of a spatial configuration of a 16-port feeding system to excite the A_2 irrep.

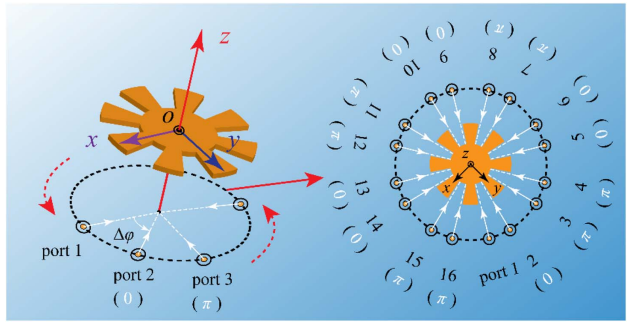

Fig. 18. Illustration of the spatial configuration of a 16-port feeding system to excite the eigen electric field belonging to the B_2 irrep.

2. Multiport Feeding Networks

Two multiport networks which are used to excite the A_2 and the B_2 irreps are illustrated in Fig. 17 and Fig. 18, respectively.

APPENDIX G: OPTIMIZATION OF THE ONE-PORT NETWORK FOR THE MAXIMAL EXCITATION OF THE *M*0 MODE

By using the symmetry-matching principle from our previous work [47,51], we find, when $r_{f1} = 4$ mm [see the definition of this parameter in Fig. 4(b) of the main text], only the electric field belonging to the A_1 irrep, i.e., the $M0$ mode, is excited (see Fig. 19 for the reflection coefficient and the field).

APPENDIX H: FURTHER DISCUSSIONS ON FIGS. 7 AND 8

First, we plot the E_L and the E_R components of the in-plane electric field in Fig. 20 and the Stokes field S_{12} in Fig. 21. In the

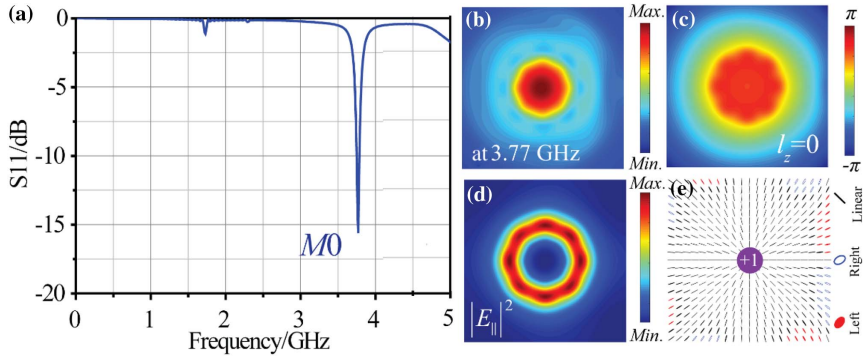

Fig. 19. Illustration of the simulated reflection coefficient S_{11} and the excited electric field. (a) shows the reflection coefficient. The magnitude and the phase of the out-of-plane component, i.e., E_z, are plotted in (b) and (c), while the intensity and the polarization distributions of the in-plane components, i.e., $\mathbf{E}_{||}$, are plotted in (d) and (e).

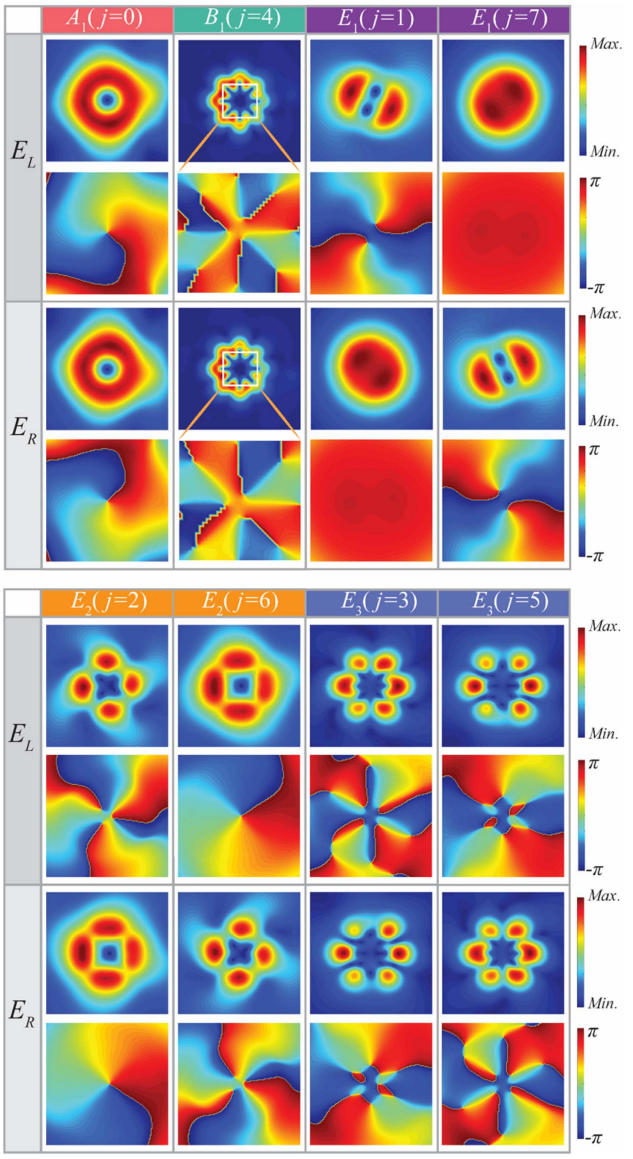

Fig. 20. Illustration of the simulated magnitude and phase distributions of the E_L and the E_R components of the in-plane electric fields. The figure includes eight columns. The columns marked by $A_1(j=0)$ and $B_1(j=4)$ correspond to Fig. 7 in the main text. The rest of the columns correspond to Fig. 8 in the main text. The figure includes two subplots. In each subplot, there are two panels. The upper panel and the lower panel correspond to the E_L and the E_R components of the in-plane eigen electric fields, respectively. The first row and the second row of the upper (lower) panel are the magnitude and the phase distributions of the E_L (E_R) component of the in-plane electric fields. All the phase distributions are zoomed-in plots in the squares encircled by white lines in the $B_1(j=4)$ column.

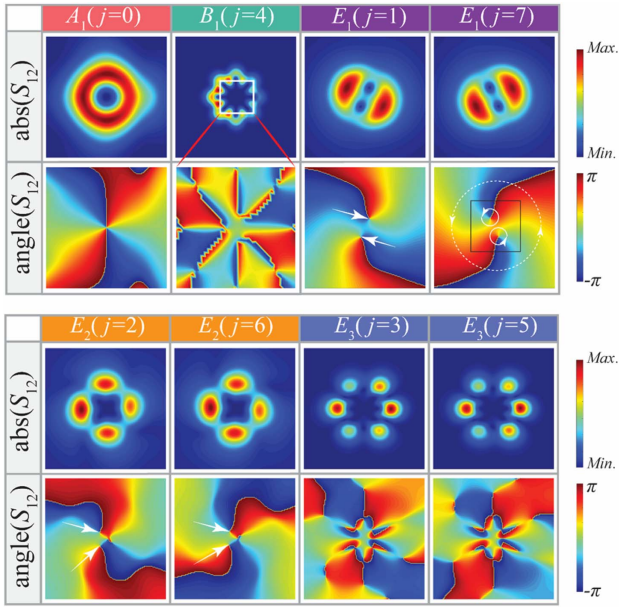

Fig. 21. Illustration of the magnitude [abs(S_{12})] and the phase [angle(S_{12})] distributions of the Stokes field S_{12}. Similar to Fig. 20, the figure consists of eight columns. The columns marked by $A_1(j=0)$ and $B_1(j=4)$ correspond to Fig. 7 in the main text. The rest of the columns correspond to Fig. 8 in the main text. Further, in the column marked by $E_1(j=7)$, a white dashed circle and two solid circles mark three loop paths. And, in the same column, a black square denotes a square region where the intensity and the polarization distributions in Fig. 23 are plotted. Additionally, in the columns marked by $E_1(j=1)$, $E_2(j=2)$, and $E_2(j=6)$, the arrows point at the C-points whose topological charge is 1/2. Lastly, all the phase distributions are plotted in the square encircled by the white line in the column marked by $B_1(j=4)$.

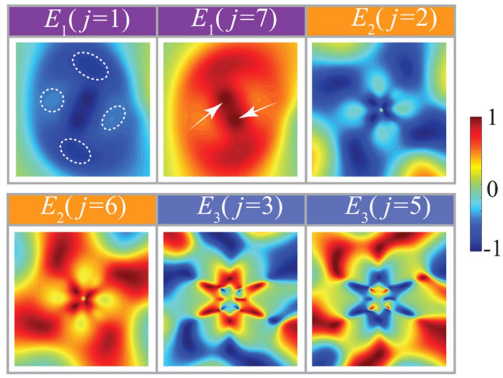

Fig. 22. Illustration of the normalized Stokes parameters S_3/S_0 corresponding to Fig. 8 in the main text. Two white arrows point at the locations where the S_3/S_0 equals 1.

two figures, the columns marked by A_1 and B_1 correspond to Fig. 7, while the columns marked by E_1, E_2, and E_3 correspond to Fig. 8.

Second, we evaluate the normalized Stokes field S_3/S_0 (see Fig. 22) to study the C-points in Fig. 8 in more detail. In the following, we focus on the plot in the column marked by $E_1(j=7)$ in Fig. 21, and similar discussions apply to other plots. The plot demonstrates a similar trend to the plot in the column marked by $E_1(j=7)$ in Fig. 10. That is, S_3/S_0 varies from 0 at the boundary to −1 at the center. However, the plot in Fig. 10 demonstrates a perfect circular shape, while its counterpart in Fig. 21 shows a deformed elliptical shape. Further, at the center of the plot in Fig. 21, S_3/S_0 is not exactly equal to −1.

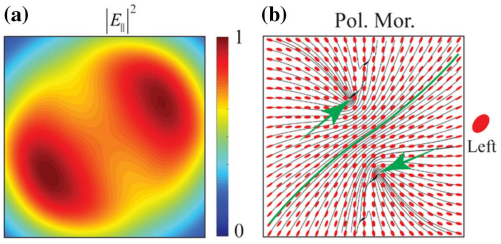

Fig. 23. Illustration of the $\mathbf{E}_{||}$ in the black square in Fig. 21. (a) Intensity; (b) polarization distribution. In (b), the black lines denote the streamlines of the local polarization states, from which it can be observed that there are two C-points with a topological charge of 1/2, as pointed at by the green arrows, and one (quasi-)L line.

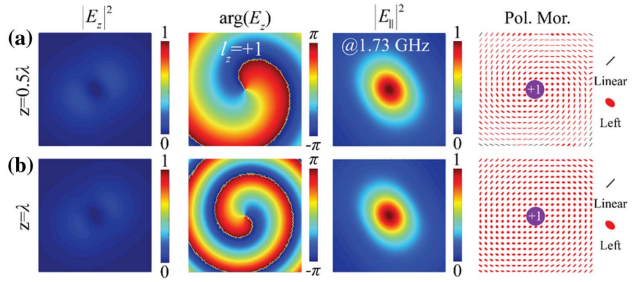

Fig. 25. Illustration of the out-of-plane and the in-plane components of the electric field radiated by the resonator in Fig. 4 of the main text. Here, the electric fields are plotted at 1.73 GHz on two cut planes. (a) $z = 0.5\lambda$ and (b) $z = \lambda$ (where λ is the vacuum wavelength corresponding to 1.73 GHz), and the electric fields belong to the $E_1(j = 7)$ irrep. In (a) and (b), the intensities of the E_z are normalized by the maximal intensities of the $\mathbf{E}_{||}$, respectively. "Pol. Mor." is the abbreviation of "polarization morphology."

These differences can be further understood by looking at the scalar vortices in the left and right components, i.e., E_L and E_R, of the in-plane fields. The E_L and the E_R related to the plot in the column marked by $E_1(j = 7)$ in Fig. 10 are plotted in the column marked by $E_1(j = 7)$ in Fig. 11. The E_L and the E_R related to the plot in the column marked by $E_1(j = 7)$ in Fig. 21 are plotted in the column marked by $E_1(j = 7)$ in Fig. 20. By comparing the E_L and the E_R components in Figs. 11 and 20, it is observed that both results demonstrate a topological charge of 0 in E_R and a topological charge of –2 in E_L (in Fig. 11, the topological charges are exact; in Fig. 20, the topological charges are approximate). However, by comparing with the results in Fig. 11, the scalar vortex mode in the E_R component in Fig. 20 does not demonstrate a maximum in the magnitude right at the center. Also, its phase distribution does not exhibit an annular shape. Further, the scalar vortex in the E_L component in Fig. 20 does not exhibit a donut-like distribution in magnitude. Nor does it form a perfect phase singularity at the center.

The main reason for the imperfection is due to the use of the two-port feeding network that breaks the symmetries of the resonator. The symmetry breaking further leads to a splitting of the C-points. To see the splitting, still focus on the columns marked by $E_1(j = 7)$ in Fig. 21 and in Fig. 22. From the phase distribution of the S_{12} in Fig. 21, it can be observed that along the white dashed loop path (denoted by a white dashed circle in Fig. 21), the winding number is 2, i.e., the topological charge carried by the scalar vortex in S_{12} is 2; however, along one of two white solid loop paths (denoted by two white solid circles in Fig. 22), the phase-winding number is 1, i.e., the topological charge is 1. This result suggests that the C-point carrying topological charge of 1 is split into two C-points with topological charge of 1/2 at the central region. The distribution of the S_3/S_0 in Fig. 22 further demonstrates that there are two points (pointed by two white arrows in Fig. 22) where the S_3/S_0 equals 1, i.e., at the two points the local polarization states are circular polarizations. We further plot the intensity and polarization distributions (see Fig. 23) of the in-plane electric field corresponding to the column marked by $E_1(j = 7)$ in Figs. 21 and 22. Figure 23 confirms the above observation on the splitting. As shown in Fig. 23(b), two C-points and one (quasi-)L line are found in the central region of the plot. Such a splitting has also been observed in previous literature [53,54], in which other perturbation mechanisms break the

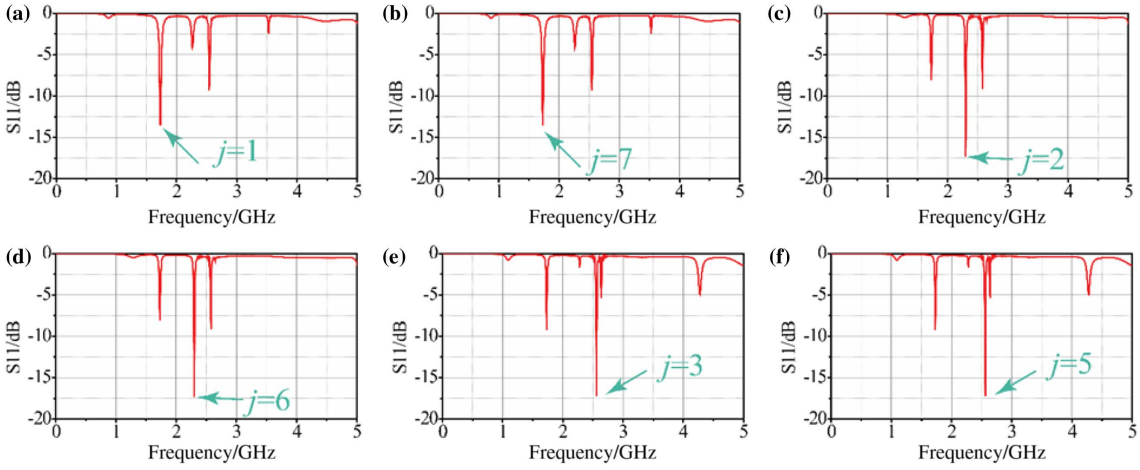

Fig. 24. Reflection coefficients S_{11} of different two-port feeding networks. The reflection coefficients S_{11} in (a)–(f) correspond to (a)–(f) in Fig. 8 of the main text. The design parameters of the two-port feeding networks can be found in the caption of Fig. 8 of the main text.

rotational symmetries and further lead to the splitting of the C-points [54].

APPENDIX I: REFLECTION COEFFICIENTS FOR DIFFERENT TWO-PORT FEEDING NETWORK DESIGNS

The reflection coefficients corresponding to Fig. 8 in the main text are shown in Fig. 24.

APPENDIX J: ELECTRIC FIELDS ON DIFFERENT *z* CUTS ABOVE THE RESONATOR

The in-plane and the out-of-plane components of the electric field radiated by the resonator in Fig. 4 are illustrated in Fig. 25.

Funding. Fonds Wetenschappelijk Onderzoek (G090017N); KU Leuven (C14/19/083, IDN/20/014, KA/20/019); National Natural Science Foundation of China (61771485, 62288101); National Key Research and Development Program of China (SQ2017YFA0700201, SQ2017YFA0700202, SQ2017YFA0700203).

Acknowledgment. T. J. Cui acknowledges the support by the National Natural Science Foundation of China. X. Zheng and G. A. E. Vandenbosch would like to thank the KU Leuven internal funds: the C1 project C14/19/083, the IDN project IDN/20/014, and the small infrastructure grant KA/20/019; and the Research Foundation of Flanders (FWO) project G090017N. X. Zheng is also grateful for the IEEE Antennas and Propagation Postdoctoral Fellowship.

Disclosures. The authors declare that they have no conflicts of interest.

Data Availability. The data that support the findings of this study are available from the corresponding author upon reasonable request.

REFERENCES

1. J. F. Nye, "Lines of circular polarization in electromagnetic wave fields," Proc. R. Soc. A **389**, 279–290 (1983).
2. J. F. Nye, "Polarization effects in the diffraction of electromagnetic waves: the role of disclinations," Proc. R. Soc. A **387**, 105–132 (1983).
3. T. Bauer, P. Banzer, E. Karimi, S. Orlov, A. Rubano, L. Marrucci, E. Santamato, R. W. Boyd, and G. Leuchs, "Observation of optical polarization Möbius strips," Science **347**, 964–966 (2015).
4. E. Pisanty, G. J. Machado, V. Vicuña-Hernández, A. Picón, A. Celi, J. P. Torres, and M. Lewenstein, "Knotting fractional order knots with the polarization state of light," Nat. Photonics **13**, 569–574 (2019).
5. L. Allen, M. W. Beijersbergen, R. J. C. Spreeuw, and J. P. Woerdman, "Orbital angular momentum of light and the transformation of Laguerre-Gaussian laser modes," Phys. Rev. A **45**, 8185–8189 (1992).
6. Y. Shen, X. Wang, Z. Xie, C. Min, X. Fu, Q. Liu, M. Gong, and X. Yuan, "Optical vortices 30 years on: OAM manipulation from topological charge to multiple singularities," Light Sci. Appl. **8**, 90 (2019).
7. G. Milione, H. I. Sztul, D. A. Nolan, and R. R. Alfano, "Higher-order Poincaré sphere, Stokes parameters, and the angular momentum of light," Phys. Rev. Lett. **107**, 053601 (2011).
8. H. M. Doeleman, F. Monticone, W. den Hollander, A. Alù, and A. F. Koenderink, "Experimental observation of a polarization vortex at an optical bound state in the continuum," Nat. Photonics **12**, 397–401 (2018).
9. B. Wang, W. Liu, M. Zhao, J. Wang, Y. Zhang, A. Chen, F. Guan, X. Liu, L. Shi, and J. Zi, "Generating optical vortex beams by momentum-space polarization vortices centred at bound states in the continuum," Nat. Photonics **14**, 623–628 (2020).
10. Z. Che, Y. Zhang, W. Liu, M. Zhao, J. Wang, W. Zhang, F. Guan, X. Liu, W. Liu, L. Shi, and J. Zi, "Polarization singularities of photonic quasicrystals in momentum space," Phys. Rev. Lett. **127**, 043901 (2021).
11. E. N. Bulgakov and D. N. Maksimov, "Bound states in the continuum and polarization singularities in periodic arrays of dielectric rods," Phys. Rev. A **96**, 063833 (2017).
12. W. Liu, W. Liu, L. Shi, and Y. Kivshar, "Topological polarization singularities in metaphotonics," Nanophotonics **10**, 1469–1486 (2021).
13. W. Chen, Y. Chen, and W. Liu, "Singularities and Poincaré indices of electromagnetic multipoles," Phys. Rev. Lett. **122**, 153907 (2019).
14. W. Chen, Y. Chen, and W. Liu, "Line singularities and Hopf indices of electromagnetic multipoles," Laser Photon. Rev. **14**, 2000049 (2020).
15. M. V. Berry and M. R. Dennis, "The optical singularities of birefringent dichroic chiral crystals," Proc. R. Soc. A **459**, 1261–1292 (2003).
16. W. Chen, Q. Yang, Y. Chen, and W. Liu, "Extremize optical chiralities through polarization singularities," Phys. Rev. Lett. **126**, 253901 (2021).
17. R. P. Senthilkumaran and S. K. Pal, "Phase singularities to polarization singularities," Int. J. Opt. **2020**, 2812803 (2020).
18. J. V. Hajnal, "Observations of singularities in the electric and magnetic fields of freely propagating microwaves," Proc. R. Soc. A **430**, 413–421 (1990).
19. A. M. Yao and M. J. Padgett, "Orbital angular momentum: origins, behavior and applications," Adv. Opt. Photon. **3**, 161–204 (2011).
20. Y. Kozawa and S. Sato, "Optical trapping of micrometer-sized dielectric particles by cylindrical vector beams," Opt. Express **18**, 10828–10833 (2010).
21. P. Shi, L. Du, and X. Yuan, "Structured spin angular momentum in highly focused cylindrical vector vortex beams for optical manipulation," Opt. Express **26**, 23449–23459 (2018).
22. G. Situ, G. Pedrini, and W. Osten, "Spiral phase filtering and orientation-selective edge detection/enhancement," J. Opt. Soc. Am. A **26**, 1788–1797 (2009).
23. B. S. B. Ram, P. Senthilkumaran, and A. Sharma, "Polarization-based spatial filtering for directional and nondirectional edge enhancement using an S-waveplate," Appl. Opt. **56**, 3171–3178 (2017).
24. B. S. B. Ram and P. Senthilkumaran, "Edge enhancement by negative Poincare–Hopf index filters," Opt. Lett. **43**, 1830–1833 (2018).
25. J. Bravo-Abad, M. Ibanescu, J. D. Joannopoulos, and M. Soljacic, "Observation of polarization singularities at the nanoscale," Phys. Rev. A **74**, 053619 (2006).
26. I. Fushman, D. Englund, A. Faraon, N. Stoltz, P. Petroff, and J. Vuckovic, "Controlled phase shifts with a single quantum dot," Science **320**, 769–772 (2008).
27. S. Tsesses, E. Ostrovsky, K. Cohen, B. Gjonaj, N. H. Lindner, and G. Bartal, "Optical skyrmion lattice in evanescent electromagnetic fields," Science **361**, 993–996 (2018).
28. L. Du, A. Yang, A. V. Zayats, and X. Yuan, "Deep-subwavelength features of photonic skyrmions in a confined electromagnetic field with orbital angular momentum," Nat. Phys. **15**, 650–654 (2019).
29. Y. Dai, Z. Zhou, A. Ghosh, R. S. K. Mong, A. Kubo, C.-B. Huang, and H. Petek, "Plasmonic topological quasiparticle on the nanometre and femtosecond scales," Nature **588**, 616–619 (2020).
30. Q. Zhang, Z. Xie, L. Du, P. Shi, and X. Yuan, "Bloch-type photonic skyrmions in optical chiral multilayers," Phys. Rev. Res. **3**, 023109 (2021).
31. S. Quabis, R. Dorn, M. Eberler, O. Glöckl, and G. Leuchs, "Focusing light to a tighter spot," Opt. Commun. **179**, 1–7 (2000).
32. R. Dorn, S. Quabis, and G. Leuchs, "Sharper focus for a radially polarized light beam," Phys. Rev. Lett. **91**, 233901 (2003).
33. L. E. Helseth, "Smallest focal hole," Opt. Commun. **257**, 1–8 (2006).
34. B. Hao, J. Burch, and J. Leger, "Smallest flattop focus by polarization engineering," Appl. Opt. **47**, 2931–2940 (2008).

35. S. M. Mohammadi, L. K. S. Daldorff, J. E. S. Bergman, R. L. Karlsson, B. Thide, K. Forozesh, T. D. Carozzi, and B. Isham, "Orbital angular momentum in radio—a system study," IEEE Trans. Antennas Propag. **58**, 565–572 (2010).
36. M. D. Williams, M. M. Coles, K. Saadi, D. S. Bradshaw, and D. L. Andrews, "Optical vortex generation from molecular chromophore arrays," Phys. Rev. Lett. **111**, 153603 (2013).
37. M. M. Coles, M. D. Williams, K. Saadi, D. S. Bradshaw, and D. L. Andrews, "Chiral nanoemitter array: a launchpad for optical vortices," Laser Photon. Rev. **7**, 1088–1092 (2013).
38. X. Cai, J. Wang, M. J. Strain, B. Johnson-Morris, J. Zhu, M. Sorel, J. L. O'Brien, M. G. Thompson, and S. Yu, "Integrated compact optical vortex beam emitters," Science **338**, 363–366 (2012).
39. P. Miao, Z. Zhang, J. Sun, W. Walasik, S. Longhi, N. M. Litchinitser, and L. Feng, "Orbital angular momentum microlaser," Science **353**, 464–467 (2016).
40. N. C. Zambon, P. St-Jean, M. Milicevic, A. Lemaître, A. Harouri, L. Le Gratiet, O. Bleu, D. D. Solnyshkov, G. Malpuech, I. Sagnes, S. Ravets, A. Amo, and J. Bloch, "Optically controlling the emission chirality of microlasers," Nat. Photonics **13**, 283–288 (2019).
41. C. Huang, C. Zhang, S. Xiao, Y. Wang, Y. Fan, Y. Liu, N. Zhang, G. Qu, H. Ji, J. Han, L. Ge, Y. Kivshar, and Q. Song, "Ultrafast control of vortex microlasers," Science **367**, 1018–1021 (2020).
42. J. Wang, J.-Y. Yang, I. M. Fazal, N. Ahmed, Y. Yan, H. Huang, Y. Ren, Y. Yue, S. Dolinar, M. Tur, and A. E. Willner, "Terabit free-space data transmission employing orbital angular momentum multiplexing," Nat. Photonics **6**, 488–496 (2012).
43. N. Bozinovic, Y. Yue, Y. Ren, M. Tur, P. Kristensen, H. Huang, A. E. Willner, and S. Ramachandran, "Terabit-scale orbital angular momentum mode division multiplexing in fibers," Science **340**, 1545–1548 (2013).
44. J. W. Zhang, J. Y. Liu, L. Shen, L. Zhang, J. Luo, J. Liu, and S. Y. Yu, "Mode-division multiplexed transmission of wavelength-division multiplexing signals over a 100-km single-span orbital angular momentum fiber," Photon. Res. **8**, 1236–1242 (2020).
45. W. Y. Tsai, J. S. Huang, and C. B. Huang, "Selective trapping or rotation of isotropic dielectric microparticles by optical near field in a plasmonic archimedes spiral," Nano Lett. **14**, 547–552 (2014).
46. B. Zhen, C. W. Hsu, L. Lu, A. D. Stone, and M. Soljačić, "Topological nature of optical bound states in the continuum," Phys. Rev. Lett. **113**, 257401 (2014).
47. J. Yang, X. Z. Zheng, J. F. Wang, Y. T. Pan, A. X. Zhang, T. J. Cui, and G. A. E. Vandenbosch, "Symmetry-protected spoof localized surface plasmonic skyrmion," Laser Photon. Rev. **16**, 2200007 (2022).
48. J.-P. Serre, *Linear Representations of Finite Groups* (Springer, 1977).
49. M. Tinkham, *Group Theory and Quantum Mechanics* (Courier, 2003).
50. J. Yang, P. Y. Feng, F. Han, X. Z. Zheng, J. F. Wang, Z. W. Jin, N. Verellen, J. C. Ni, W. J. Chen, Y. J. Yang, A. X. Zhang, C. W. Qiu, and G. A. E. Vandenbosch, "Symmetry-compatible angular momentum conservation relation in plasmonic vortex lenses with rotational symmetries," arXiv, arXiv:2209.14735 (2022).
51. J. Yang, X. Z. Zheng, J. F. Wang, A. X. Zhang, T. J. Cui, and G. A. E. Vandenbosch, "Customizing the topological charges of vortex modes by exploiting symmetry principles," Laser Photon. Rev. **16**, 2100373 (2022).
52. Q. Wang, C. H. Tu, Y. N. Li, and H. T. Wang, "Polarization singularities: progress, fundamental physics, and prospects," APL Photon. **6**, 040901 (2021).
53. I. Freund, "Möbius strips and twisted ribbons in intersecting Gauss-Laguerre beams," Opt. Commun. **284**, 3816–3845 (2011).
54. X. Lu, Z. Wu, W. Zhang, and L. Chen, "Polarization singularities and orbital angular momentum sidebands from rotational symmetry broken by the Pockels effect," Sci. Rep. **4**, 4865 (2014).